CHALMERS
UNIVERSITY OF TECHNOLOGY

MRI Compatible Retention System for a Bone Conduction Device

An evaluation of required design changes to Sentio Ti™ Implant for compliance with 3 T MRI scans

Master's thesis in Biomedical Engineering

MATILDA ALEXANDERSSON
EBBA LUTTU

DEPARTMENT OF ELECTRICAL ENGINEERING
CHALMERS UNIVERSITY OF TECHNOLOGY
Gothenburg, Sweden 2026
www.chalmers.se

Master's thesis 2026

MRI Compatible Retention System for a Bone Conduction Device

An evaluation of required design changes to Sentio Ti™ Implant for compliance with 3 T MRI scans

MATILDA ALEXANDERSSON
EBBA LUTTU

CHALMERS
UNIVERSITY OF TECHNOLOGY

Department of Electrical Engineering
Division of Signal Processing and Biomedical Engineering
Chalmers University of Technology
Gothenburg, Sweden 2026

MRI Compatible Retention System for a Bone Conduction Device
An evaluation of required design changes to Sentio Ti™ Implant for compliance with 3 T MRI scans
MATILDA ALEXANDERSSON
EBBA LUTTU

Supervisor: Martin Johansson & Nicole Al Hanna, Oticon Medical AB
Examiner: Karl-Johan Fredén Jansson, Electrical Engineering

Master's Thesis 2026
Department of Electrical Engineering
Division of Signal Processing and Biomedical Engineering
Chalmers University of Technology
SE-412 96 Gothenburg
Telephone +46 31 772 1000

Cover: Sentio Ti™ bone conduction implant, Oticon Medical

Typeset in LaTeX
Printed by Chalmers Reproservice
Gothenburg, Sweden 2026

MRI Compatible Retention System for a Bone Conduction Device
An evaluation of required design changes to Sentio Ti™ Implant for compliance with 3 T MRI scans
MATILDA ALEXANDERSSON
EBBA LUTTU
Department of Electrical Engineering
Chalmers University of Technology

Abstract

Magnetic resonance imaging (MRI) compatibility is an important requirement for implantable hearing devices, as increasing numbers of patients are expected to undergo MRI examinations during their lifetime. This study evaluates the mechanical response of the Sentio Ti™ transcutaneous bone conduction implant under magnetic torque corresponding to a 3 T MRI environment, with the aim of assessing whether the current design meets established performance criteria defined at 1.5 T. A computational approach was conducted using an existing, experimentally validated finite element model developed in LS-DYNA. The model was used to simulate implant displacement and contact pressure on surrounding soft tissue under worst-case magnetic torque conditions. The torque at 3 T was estimated based on proportional scaling from 1.5 T. Parametric studies were conducted to investigate the influence of reinforcement wire properties and silicone stiffness on implant behaviour. In addition, alternative retention magnet concepts were explored through a concept generation process. The results show that increasing the magnetic field strength from 1.5 T to 3 T leads to a significant increase in mechanical response, with displacement rising from 3.12 mm to 5.65 mm and average contact pressure increasing by a factor of approximately 2–3. Among the investigated parameters, reinforcement wire diameter was found to have the greatest influence on reducing both displacement and contact pressure. However, achieving equivalent performance to 1.5 T through structural modifications alone requires design changes that may be impractical within current geometric constraints. Combined modifications of wire diameter and silicone stiffness provided more feasible solutions, although they did not fully replicate baseline pressure levels. The findings indicate that while structural optimization can significantly improve performance, it may not be sufficient to ensure MRI compatibility at 3 T without compromising design constraints. Modifications to the retention magnet system, such as enabling rotational alignment or controlled movement, are therefore identified as promising strategies. This work provides quantitative insight into implant behaviour at higher magnetic field strengths and supports the development of next-generation MRI-compatible bone conduction devices.

Keywords: MRI compatibility, bone conduction, transcutaneous implant, magnetic torque, FEM, LS-Dyna, contact pressure, implant displacement, retention magnet, Sentio Ti™

Acknowledgements

We would like to express our greatest thankfulness to everyone who contributed to the completion of this thesis. This project would not have been possible without you.

First and foremost, we are extremely grateful to Oticon Medical for giving us the opportunity to conduct our thesis within the company and want to thank everyone at the office in Askim for a friendly and helpful working environment. We especially want to thank our internal supervisor Nicole Al Hanna who consistently put up with our questions during the semester and helped guiding us through this project. We also want to thank Martin Johansson and Marsel Ganeyev for their time and valuable expertise. It has been a great experience where we have gained many new insights and hands-on experience.

We would also like to thank our examiner and supervisor at Chalmers, Karl-Johan Fredén Jansson, who came with valuable input and great support during the project.

Lastly, we are thankful for the help and support from FS Dynamics, especially our contact person Cyrus Nilsson who has provided significant help with computing the simulations and with our understanding of them.

Matilda Alexandersson & Ebba Luttu, Gothenburg, May 2026

List of Acronyms

Below is the list of acronyms that have been used throughout this thesis listed in alphabetical order:

AC	Air Conduction
BC	Bone Conduction
CROS	Contralateral routing of signal
FEM	Finite Element Method
HSO	Hardened Silicone Overmold
MR	Magnetic Resonance
MRI	Magnetic Resonance Imaging
PPT	Pressure Pain Threshold
RF	Radiofrequency
SAR	Specific absorbtion rate
SNR	Signal-to-noise ratio
SNHL	Sensorineural hearing loss
SSD	Single-sided deafness

Nomenclature

B_0	Static magnetic field (MRI field strength)
∇B_0	Magnetic field gradient
F_{trans}	Translational magnetic force
m	Magnetic dipole moment
τ	Magnetic torque
E	Young's modulus
S	Shore A hardness
C_{10}, C_{01}	Mooney–Rivlin material parameters
$M(x)$	Bending moment along the beam
I	Area moment of inertia
$\kappa(x)$	Curvature of the beam
μ	Magnetic permeability
μ_0	Permeability in vacuum
M	Magnetization
B_r	Remanent flux density
B	Magnetic flux density
H	Magnetic field strength
H_c	Coercive field

Contents

List of Figures

List of Tables

1

Introduction

Hearing loss is a growing global problem and the World Health Organization (WHO) estimates that by 2050, 2.5 billion people worldwide will have some degree of hearing loss, of whom more than 700 million will require some form of hearing rehabilitation or hearing aid [1]. Without appropriate aid, hearing loss can impair communication and negatively affect quality of life, as well as educational and professional opportunities. Hearing loss may be congenital or acquired and depending on the underlying cause, different types of hearing aids are used. There are three main types of hearing loss treatments; conventional hearing aids, cochlear implants and bone conduction systems. The latter are meant for patients with conductive, mixed hearing loss or single-sided deafness. These systems are available in both percutaneous and transcutaneous forms. Percutaneous implants involve a direct connection to the skull via an abutment anchored in the bone that penetrates the skin. Transcutaneous solutions, on the other hand, transmit vibrations to the inner ear via an implanted transducer while keeping the skin intact. These implants include a permanent retention magnet, which may lead to compatibility issues during Magnetic Resonance Imaging (MRI) examinations. As these examinations become increasingly common, individuals with hearing implants are likely to require at least one MRI scan during their lifetime [2]. Considering this, ensuring MRI compatibility is essential for maintaining equal access to medical diagnostics. Oticon Medical AB (Askim, Sweden) is therefore working to improve the MRI robustness of their transcutaneous bone conduction implant, Sentio Ti™.

1.1 Background

The Sentio™ system, developed by Oticon Medical AB, is a transcutaneous bone conduction system intended for patients with conductive or mixed hearing loss and single-sided deafness [3]. The system consists of an external sound processor and an implant positioned beneath the skin, see Figure 1.1.

Figure 1.1: Sentio system including external sound processor and Sentio Ti™ implant. Image provided by Oticon Medical.

The implant is surgically positioned behind the ear and consists of a transducer anchored to the skull and an antenna part overmolded by silicone. The antenna part contains a receiver coil, magnet housing and a permanent retention magnet, which enables coupling to the external sound processor. In this report, the term Sentio refers to Sentio Ti™, i.e. the implant. The term antenna refers to the entire flexible part overmolded by silicone, including the coils, retention magnet and reinforcement wire, see Figure 1.2.

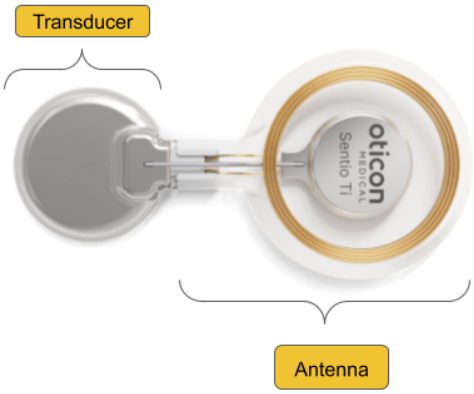

Figure 1.2: The Sentio Ti™ implant consisting of a bone-anchored transducer and an antenna, from Oticon Medical.

In a MRI examination, the strong magnetic fields can induce forces and torque in implants, especially in components containing permanent magnets [4]. In the Sentio Ti™ implant, the retention magnet is therefore expected to be the most susceptible component to mechanical displacement.

Previous work has investigated the behaviour of the implant under MRI conditions. Bench tests conducted by Oticon Medical were used as the basis for the previously

performed simulations. These simulations showed that the implant experiences displacement when exposed to a magnetic field of 1.5 Tesla (T). Clinical testing reported no severe discomfort, and the implant is now FDA-approved and conditionally approved for MRI scans at 1.5 T.

However, higher magnetic field strengths such as 3 T are increasingly used in clinical practice [5]. At these field strengths the induced magnetic torque on the implant increases. This can lead to greater displacement of the antenna and higher mechanical loading on the surrounding tissue, potentially leading to pain or rupture of overlying tissues.

While Sentio is conditionally approved for MRI at 1.5 T, its mechanical response under 3 T conditions remains unknown. In particular, the resulting displacement and tissue loading due to increased magnetic torque have not been quantitatively assessed. Further investigation and improvement of the MRI robustness of the implant is required to get it approved for MRI scans of 3 T.

1.2 Aim

Through the use of computer modelling and theoretical calculations, this project aims to evaluate the mechanical response of the Sentio implant under 3 T MRI conditions. Specifically, the study will quantify implant displacement and contact pressure on surrounding tissue and compare these results with existing data at 1.5 T. Based on these findings, the study will assess whether design modifications to the retention magnet system are required to achieve MRI compatibility at 3 T without exceeding the mechanical limits observed at 1.5 T. The project will generate quantitative data on how the implant behaves at magnetic field strengths of 3 T, and provide input to the future strategies on the development of next-generation transcutaneous bone conduction devices.

A key challenge of this project will be to enhance MRI performance while preserving the functional and design advantages of the current system, as required by Oticon Medical. The issue being investigated is specified by the following questions:

- What are the worst-case displacement and contact pressure on surrounding tissue experienced by the implant under torque corresponding to 3 T MRI conditions, and how do these compare to 1.5 T MRI?

- What design changes of the implant, except for the magnet itself, are needed to maintain displacement and contact pressure equal to those at 1.5 T?

- What alternative retention magnet concepts could enable MRI compatibility at 3 T for this particular transcutaneous implant design?

1.3 Limitations

This study is limited to the evaluation of the retention magnet system and how it affects the antenna of the implant under 3 T MRI conditions. The bone-anchored transducer component and the external sound processor will be excluded.

The study focuses on the induced torque acting on the implant in the isocentre of the MRI bore. Only the static magnetic field B_0 will be considered, while the effects of radiofrequency fields and time-varying gradient fields are neglected due to their comparatively smaller contribution to mechanical torque.

This is a computational study that will be based solely on literature review, simulations and concept generation. It does not include bench testing or experimental validation, nor does it include any experiments on real patients. However, the already existing computational model is validated from bench tests and is therefore considered appropriate.

A simplified representation of the implant was used in the computer simulations. It was developed in collaboration between Oticon Medical and FS Dynamics based on the implant's behavior in a bench test corresponding to a 1.5 T MRI scan. The model does not include magnetic properties, instead, it takes torque as input and yields mechanical behaviour as output. The torque used in the simulations corresponds to the worst-case scenario, that is, when the B_0 field and the retention magnet is completely perpendicular. No other angles between magnet and B_0 will be investigated. The magnetic field inside the bore is assumed to be horizontal and can have either positive or negative direction along the z-axis.

This project will strive for the implant to be conditionally approved and the conditions will be assumed to be the same as for the current implant in 1.5 T. Importantly, during this work, no other possible MRI incompatibility issues such as demagnetization, induced sound, heating or the impact of 3 T on the transducer have been considered.

2

Theory

This chapter introduces necessary concepts for this project, including the auditory organ, conduction of sound, hearing loss and corresponding aids, MRI, medical implants and magnetic materials.

2.1 The Auditory Organ

The auditory organ is responsible for detecting, transmitting and processing sound [6]. It is anatomically divided into the outer ear, the middle ear and the inner ear, as illustrated in Figure 2.1 below.

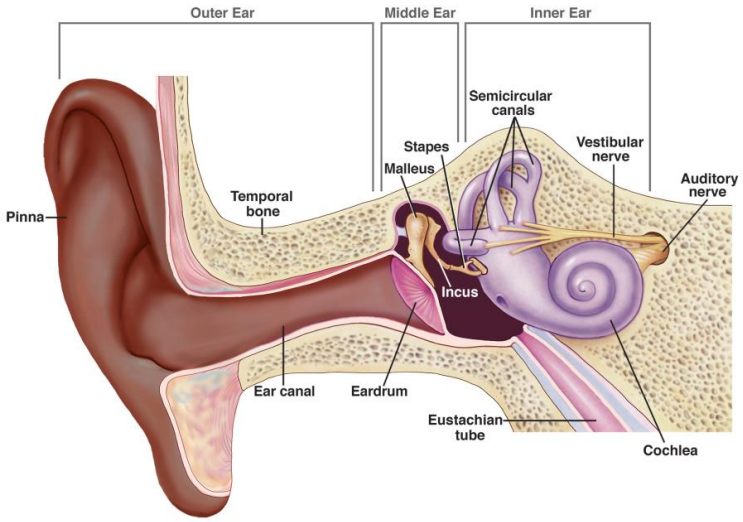

Figure 2.1: Anatomy of the human ear, from [7].

Sound waves are first collected by the outer ear and guided through the ear canal to the eardrum. The resulting eardrum vibrations are transmitted through the middle ear by the ossicular chain, consisting of the malleus, incus and stapes before entering the oval window of the cochlea [8].

The middle ear acts as an impedance matching system that transfers sound vibrations from air to the fluid-filled inner ear [9]. Vibrations of the stapes at the oval window create fluid motion inside the cochlea where mechanical vibrations are con-

verted into electrical signals by sensory hair cells [6].

These electrical signals are transmitted through the auditory nerve to the brainstem and further to the auditory cortex, where sound is processed and perceived [6].

2.2 Conduction of Sound

Sound vibrations can reach the inner ear and cochlea in three main ways: air conduction (AC), bone conduction (BC) and body conduction [10]. As illustrated in Figure 2.2, AC is the primary way sound is perceived and occurs when sound travels through the ear canal to the cochlea. BC occurs when vibrations are transmitted through the skull bone directly to the cochlea, while body conduction refers to vibrations transmitted through the skeleton, fluids and soft tissue in the body.

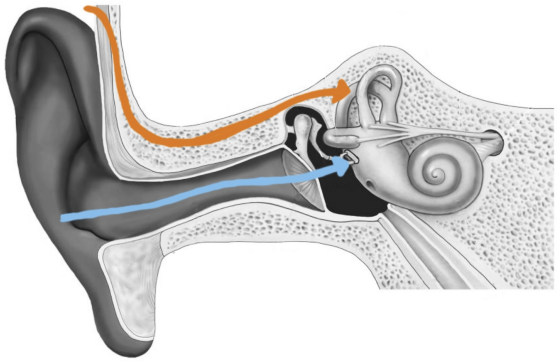

Figure 2.2: Illustration of sound transmission to the cochlea via AC (blue) and BC (orange). Adapted from [7].

Environmental vibrations can also induce vibrations in the skull, creating a BC component in hearing [11]. In a healthy ear, where sound is efficiently transmitted through AC, the BC component is generally negligible compared to AC.

However, BC provides an alternative pathway for sound to reach the cochlea and can therefore be beneficial for individuals with conductive hearing impairments [12]. In this case, vibrations are transmitted through the skull bone rather than the ear canal and are converted into fluid motion in the cochlea, enabling sound perception in a similar way to AC [13].

When a person vocalizes, they perceive their own voice through both AC and BC [14]. Sound travels through the air into the ear canal, but vibrations also reach the inner ear through the skull, including the vocal cords and teeth. When the voice is recorded and played back to the person, it often sounds different because the BC component is absent and only the AC component is heard.

2.3 Hearing Loss

Hearing loss can be both congenital or acquired later in life [15]. It is mainly classified into sensorineural, conductive or mixed hearing loss. Other forms also occur, such as single-sided deafness (SSD). Sensorineural hearing loss (SNHL) is the most common form of permanent hearing loss, accounting for approximately 90% of all cases [16]. SNHL occurs when the sensory hair cells in the cochlea or the auditory nerve are damaged. This usually happens due to aging or noise-related trauma, and is generally irreversible.

In contrast, conductive hearing loss results from dysfunction in the outer or middle ear that prevents sound from being efficiently transmitted to the inner ear while the sensory hair cells remain intact [17]. Congenital cases are typically associated with malformations of the outer or middle ear [18], while acquired conductive hearing loss is most often related to infections, trauma, or degenerative changes [19]. A conductive hearing loss is in many cases treatable by surgery or prostheses. Figure 2.3 illustrates where the dysfunction is located in the auditory organ for both SNHL and conductive hearing loss.

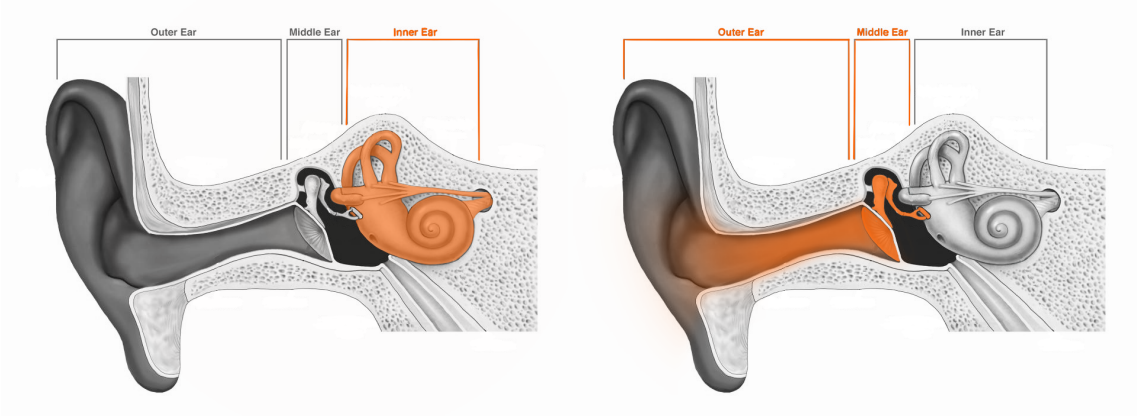

(a) SNHL, located in inner ear. Adapted from [7].

(b) Conductive hearing loss, located in middle or outer ear. Adapted from [7].

Figure 2.3: Location of sensorineural vs conductive hearing loss.

Mixed hearing loss refers to a combination of both sensorineural and conductive components, where both the sound transmission pathway and the inner ear are affected [20]. It may occur when a person with pre-existing SNHL develops an additional conductive component, such as middle ear infection or effusion [21]. It may also result from trauma, chronic ear disease or congenital abnormalities affecting multiple parts of the auditory system.

SSD is characterized by severe-to-profound hearing loss in one ear while hearing in the contralateral ear remains normal or near normal [22]. Treatments of SSD focuses on improving functional hearing and options include contralateral routing

of signal (CROS) hearing aids, bone conduction devices, or cochlear implants in selected cases [22]. The choice of hearing aid depends on the etiology of the hearing loss, duration of deafness, and individual listening needs.

2.4 Hearing Aids

Hearing aids are used to support people with different types of hearing loss, and the choice of aid depends on the type and severity of the hearing impairment.

AC hearing aids amplifies the sound and delivers it through the ear canal to the eardrum [23]. These devices rely on the natural sound transmission pathway through the outer and middle ear and are therefore mainly used for SNHL. Another alternative for SNHL is cochlear implants, a solution typically used for patients with profound deafness.

For patients with a conductive hearing loss, BC hearing aids can be used [24]. These devices transmit sound to the cochlea through vibrations of the skull, thereby bypassing the outer and middle ear.

BC systems exist in both non-implantable and implantable forms [25]. Non-implantable devices, such as softband systems, are mainly used in children or as a temporary solution to evaluate BC hearing before surgery [26]. Implantable systems can be categorized as either percutaneous or transcutaneous [25]. Percutaneous implants involve a direct connection to the skull via a titanium implant anchored in the bone with an attached abutment that penetrates the skin. Figure 2.4 illustrates how sound vibrations are transmitted to the inner ear through the implant anchored in the skull. However, permanent penetration of the skin is associated with an increased risk of complications, such as infection and inflammation. To overcome these limitations, transcutaneous implants have been developed.

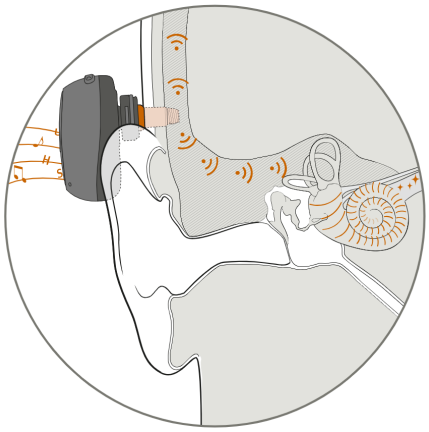

Figure 2.4: A percutaneous bone anchored hearing aid, image provided by Oticon Medical.

2.4.1 Transcutaneous Bone Conduction Implants

Transcutaneous BC implants transmit sound to the inner ear while keeping the skin intact [25]. The system consists of an external sound processor and an implant, see Figure 2.5.

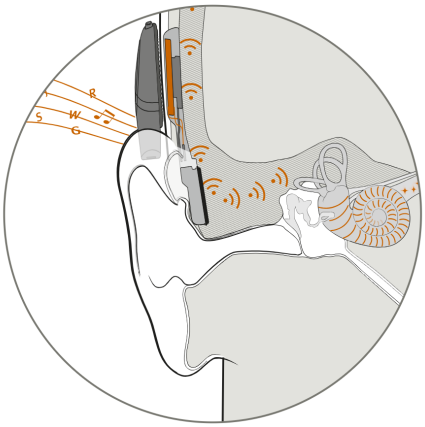

Figure 2.5: Transcutaneous bone anchored hearing aid, image provided by Oticon Medical.

The external sound processor contains a microphone that capture incoming sound and convert it into an electrical signal [24]. The processor is held in place on the skin by a magnet that couples to a corresponding retention magnet inside the implant [25]. Signal transmission between the external processor and the implant occurs through inductive coupling using a transmitter and a receiver coil. The transducer in the implant receives power and sound signals through the inductive coupling from the externally worn sound processor.

Inside the implant, the electrical signal is converted into mechanical vibrations by the transducer attached to the skull bone [24]. These vibrations are then transmitted through the skull to the cochlea via BC.

2.4.2 Transcutaneous Solutions on the Market

There are three companies on the market of BC hearing aids; Cochlear (Sydney, Australia), MED-EL (Innsbruck, Austria) and Oticon Medical (Askim, Sweden). Each company has their own active transcutaneous solution with the same principle but they all work slightly different. All solutions involve a subcutaneous implant that consists of an antenna overmolded by silicone, a transducer part in titanium attached to the bone, as well as an external sound processor held in place by a magnet. The transducer part of the implant is anchored to the mastoid part of the temporal bone and the antenna is connected to the sound processor using magnetic retention.

2.4.2.1 Cochlear Osia

The transducer part of Osia® consists of the OSI300 implant that is attached with a fixation screw to the bone-anchored BI300 implant [27]. Osia® is the only active transcutaneous BC system that is conditionally approved for MRI scans in magnetic field strengths of both 1.5 T and 3 T, with magnet in place. The magnet cassette contains a diametric magnet that rotates within its casing and can thereby align with the external magnetic field [28]. In that way it reduces any movement of the implant due to magnetically induced torque. Its system output frequency range is between 400 Hz - 7000 Hz [27].

2.4.2.2 MED-EL Bonebridge

Similar to Sentio, Bonebridge™ is conditionally approved for MRI scans at 1.5 T magnetic field strength [29]. The sound processor has a bandwidth of 250 - 8000 Hz. Bonebridge™ has a flexible design to fit different anatomies, and the transition between the transducer and the receiver coil can bend up to 90° in any lateral direction. It can also bend up to 30° medially to fit to the curvature of the skull. In that way, it can be placed at many different positions on the temporal bone, depending on anatomical circumstances.

2.4.2.3 Oticon Medical Sentio

The Sentio system consists of the Sentio Ti™ implant, placed under the skin, combined with Sentio 1 Mini sound processor outside of the skin. It is the smallest transcutaneous sound processor on the market with a bandwidth of 200-9500 Hz, as well as the smallest implant on the market [30].

Around the retention magnet there is a surrounding receiver coil, and the entire implant has an overmolded silicone rubber apart from the bottom part of the transducer casing, see Figure 2.6. The bone-anchored transducer is fixated using a flexible fixation band that is attached to the skull bone with two small fixation screws, engaging 2.7 mm into the bone [31]. Between the two parts of the implant there is a flexible implant neck with a reinforcement wire and overmolded silicone rubber that can bend up to 30° in each direction.

The retention magnet is a fixed permanent magnet and the implant is therefore at risk of movement from torques acting on the implant as well as demagnetization of the magnet if the patient undergoes an MRI. Currently, Sentio is approved for MRI scans under specific conditions, namely static magnetic field strength of 1.5 T only. If the patient requires an MRI scan of 3 T or higher, the implant needs to be taken out before the examination.

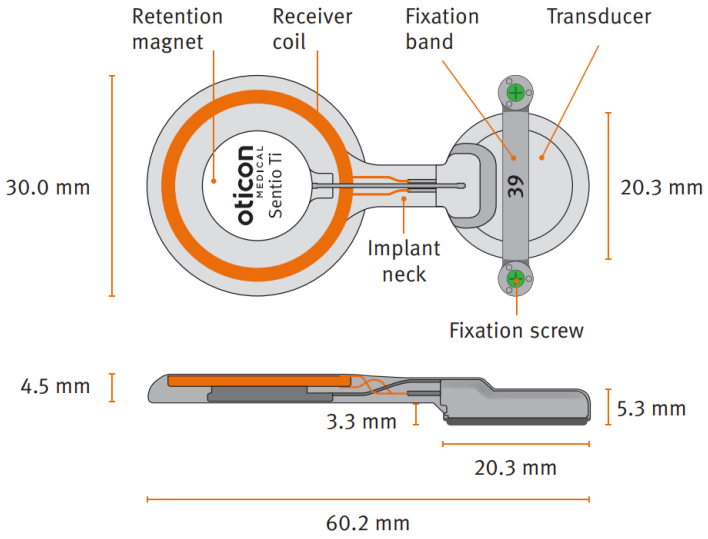

Figure 2.6: Components of the Sentio Ti™ Implant, from [32].

2.5 Magnetic Resonance Imaging

MRI is a non-invasive method of medical imaging. It differs from other scanning methods as it does not expose the patient to any ionizing radiation while providing high resolution images of the tissues in the body [33]. The following section describes the main principles of how it works.

2.5.1 Basic Principles of MRI

MRI is based on the magnetic properties of hydrogen nuclei in the human body [34]. The hydrogen nucleus consists of a single proton, which has a quantum spin and a magnetic dipole moment. Because of this magnetic moment, the proton behaves like a tiny magnet. Hydrogen is well suited for MRI because it is abundant in biological tissue, as the human body consists largely of water and each water molecule contains two hydrogen atoms.

A clinical MRI scanner consists of three main hardware components: the main magnet, the gradient coils, and the radiofrequency (RF) coils [34]. Figure 2.7 shows the MRI scanner together with the bore where the patient is positioned.

Figure 2.7: MRI scanner, from [35].

The main magnet generates a strong and uniform static magnetic field referred to as B_0. When a person is positioned in the centre of the magnetic field inside the bore, the magnetic moments of the hydrogen atoms in the body experience a torque [34]. This causes the hydrogen atoms to align either parallel or anti-parallel to the magnetic field. A small excess of protons will align parallel to the magnetic field, resulting in a net magnetization in the direction of B_0.

In addition to this alignment, the proton magnetic moments rotate around the magnetic field direction in a motion called precession [34]. To generate a measurable signal, a RF pulse is applied to disturb the net magnetization and creates a component perpendicular to B_0. When the RF pulse is switched off, the protons will return to align with B_0 through a process called relaxation. This induces a time-varying electrical signal detected by RF receiver coils. The relaxation time depends on tissue properties which is used to create contrast in MRI images.

To form an image, spatial information must be added to the signal [34]. This is achieved using magnetic field gradients from gradient coils inside the main magnet. By rapidly switching these gradients on and off, the gradients make the precession frequency position dependent. This allows the MRI signal to be spatially encoded and reconstructed into an image.

2.5.2 Magnetic Field Strength: 1.5 T vs 3 T

Clinical MRI systems most commonly operate at magnetic field strengths of 1.5 T or 3 T [34]. A higher magnetic field strength leads to an increased signal-to-noise ratio (SNR), which can be used to improve image resolution or reduce scan time [36]. For this reason, 3 T systems can provide better visualization of certain anatomical structures compared to 1.5 T systems.

Higher field strength is not always advantageous, and the choice between 1.5 T and

3 T depends on the specific imaging task and availability at the hospital [37]. At 3 T, magnetic susceptibility effects are stronger which can lead to increased image artifacts. This usually happens near air–tissue interfaces and in the presence of metallic implants. In addition, higher field strengths require stronger RF pulses, which leads to increased energy absorption in the body. This increases the specific absorption rate (SAR), a measure of the RF energy absorbed by body tissue, which can limit how RF pulses are applied and may restrict scan settings.

Higher field strengths are also associated with increased acoustic noise during scanning [37]. In addition, strong magnetic fields may cause temporary discomfort in some patients, such as dizziness or nausea [38].

2.6 Medical Implants in the MRI Environment

Medical implants are exposed to several electromagnetic fields during an MRI examination, including the static magnetic field, the RF field, and the time-varying gradient fields. These fields may interact with implants in different ways, depending on factors such as the material properties, electrical conductivity, geometry, implant location, and the strength of the MRI system.

2.6.1 Static Magnetic Field Interactions

The static magnetic field in MRI interacts with implants containing ferromagnetic materials, i.e. materials that are strongly attracted to magnetic fields, and produces mechanical forces and torque [39]. These interactions depend on the magnetic susceptibility of the material as well as the strength and spatial variation of the magnetic field.

2.6.1.1 Translational Force

Translational forces arise from spatial variations in the magnetic field and act to move an implant toward regions of higher magnetic field strength [39]. The magnitude of this force depends on the magnetic properties of the material and the spatial gradient of the magnetic field B_0. These forces are typically strongest near the entrance of the MRI bore where the field gradient ∇B_0 is largest [40]. As the object then approaches the isocentre, the magnetic field becomes more uniform and the translational force decreases.

For an object that can be approximated as a magnetic dipole, the translational force F_{Trans} can be expressed as:

$$F_{Trans} = m \cdot \nabla B_0 \tag{2.1}$$

where m is the magnetic dipole moment and ∇B_0 is the spatial gradient of the static magnetic field.

2.6.1.2 Magnetic Torque

Implants with magnetic moments may also experience torque in the presence of the static magnetic field. Unlike translational forces, torque depends on the magnetic field strength rather than the field gradient [40]. This torque tends to rotate the implant so that the magnet aligns with the main magnetic field [39], see Figure 2.8 below.

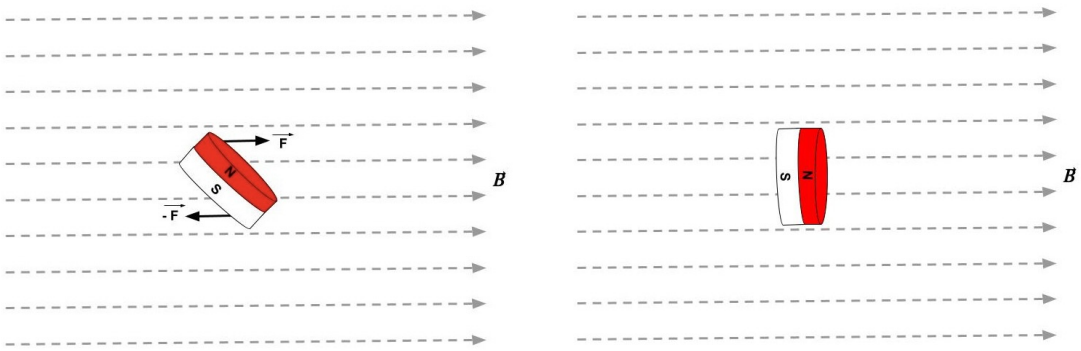

(a) Magnet in magnetic field. **(b)** Magnet aligned with magnetic field.

Figure 2.8: Torque forces acting on a magnet in an external magnetic field, resulting in magnet aligning with the field.

The magnetic torque τ acting on an object with magnetic moment m in a magnetic field B_0 can be expressed as:

$$\tau = m \times B_0 \tag{2.2}$$

The magnitude of the torque can also be written as:

$$\tau = mB_0 \sin\theta \tag{2.3}$$

where θ is the angle between the magnetic moment and the magnetic field, which means that the absolute maximum torque occur at $\pm 90°$.

2.6.1.3 Other Static Field Effects

Metallic implants can distort the static magnetic field and produce image artifacts such as signal loss or geometric distortion [41]. For implants containing permanent magnets, exposure to the static magnetic field can also lead to demagnetization depending on the field strength, the magnetic material and the orientation between the external field and the magnetization vector [42]. This may reduce the magnetic strength and affect the mechanical retention or performance of the device.

2.6.2 Radiofrequency Field Interactions

During MRI examinations, the transmitted RF energy is absorbed by the patient's tissue and converted into heat through electromagnetic induction [39]. The amount

of absorbed energy is quantified by the SAR, expressed in W/kg. Conductive medical implants can interact with the RF field and induce electrical currents. In elongated conductive structures, such as leads or wires, resonant behavior may occur and cause localized heating. The risk of RF-induced heating depends on several factors, including the RF wavelength, the geometry of the implant and its position within the RF field.

2.6.3 Time-Varying Gradient Magnetic Field Effects

The time-varying gradient magnetic fields used for spatial encoding in MRI can induce electric fields in the body [39]. These electric fields can generate currents in tissue and can lead to peripheral nerve stimulation. In patients with conductive implants, gradient-induced currents can also occur in the device, especially in leads or wires. This can increase the risk of nerve stimulation or interfere with the function of active implants. The induced currents can also cause mechanical torque or vibration of the implant. Heating from gradient-induced currents is generally lower than RF-induced heating, but mechanical vibration can still be a potential safety concern.

2.6.4 MRI Safety Classification of Medical Implants

The MRI safety classification of medical implants is defined by the ASTM F2503 standard [43], which specifies the terminology and labeling used for medical devices in the magnetic resonance (MR) environment. According to this standard, devices are classified as MR Safe, MR Conditional or MR Unsafe. MR Safe devices are composed of non-metallic, non-conductive, and non-magnetic materials and are not associated with known risks in the MR environment. MR Conditional devices have been demonstrated to be safe under specific MRI conditions, such as limits on static magnetic field strength, spatial magnetic field gradient, RF exposure or SAR. In contrast, MR Unsafe devices are associated with unacceptable risks in the MR environment, such as strong magnetic forces, excessive heating, or device malfunction and must therefore not enter the MRI scanner room.

2.6.5 Sentio in the MRI Environment

During MRI examinations, the static magnetic field interacts with the magnetic moment of the retention magnet and generates a torque that attempts to align the magnet with the external magnetic field. Since the antenna is allowed to move and the magnet cannot freely align, the torque instead causes deformation of the surrounding silicone and thereby tissue. As a result, the magnet is pushed upward within the antenna while the antenna itself can partially lift from the skull surface, leading to a displacement of the antenna relative to the bone, pushing the skin upwards. Figure 2.9 illustrates the direction in which the antenna attempts to move under the applied worst-case torque. However, the illustration is intended for conceptual understanding and does not represent the actual magnitude of the motion. The magnet is encapsulated within the silicone of the antenna and cannot detach or leave the implant.

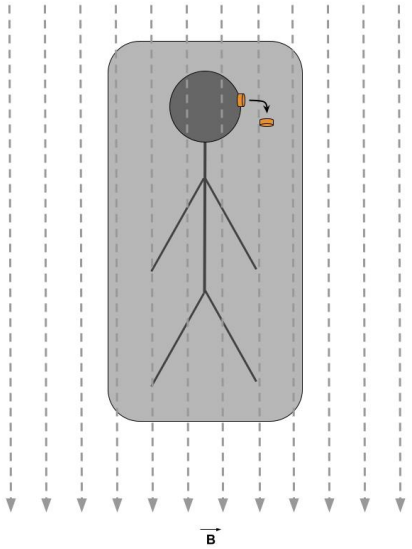

Figure 2.9: Torque acting on transcutaneous implant with permanent magnet. This is how the implant ”wants” to move.

2.7 Materials in Medical Implants

The materials used in medical implants needs to fulfil certain property requirements [44]. The implant needs to be made of a biocompatible material that does not affect the function of the implant. Other requirements of the material to take into consideration are durability, cost, and feasible fabrication and production.

2.7.1 Biocompatibility

Biocompatibility refers to a materials ability to perform as wanted in the body without causing any harm to the tissue, inflammatory reaction or damage to the material [44]. The biocompatibility of a material should always be evaluated based on its intended use, i.e. there is no such thing as a biocompatible material in general [45]. The biocompatibility of materials used in implants are evaluated based on the person and surrounding tissue in the body at wanted implant site.

2.7.1.1 Young’s Modulus (E)

For an implant to be biocompatible, it is often desirable for it to have similar stiffness as the surrounding tissue [46]. In other words, the material should have a similar Young’s modulus, or elastic modulus, as the surrounding tissue. Young’s modulus E describes the relationship between the stress and strain of a material during deformation and thus quantizes the resistance of the material when being stretched

or compressed [47]. For example, titanium is a relatively stiff material with a Young's modulus of around 105 GPa, while a soft and flexible material such as a silicone rubber behaves completely different and has a low modulus of around 1-10 MPa.

2.7.1.2 Materials used in Clinical Practice

Titanium is widely used in medical implants due to its ductility, durability, and corrosion resistance [44]. Furthermore, it is non-ferromagnetic and therefore generally compatible with MRI scans. Titanium promotes osseointegration and is therefore considered standard for bone implants. Although its elastic modulus is closer to that of cortical bone than many other metals, ongoing research aims to develop titanium alloys with an even lower modulus to further reduce mechanical mismatch [48]. The elastic modulus of cortical bone is approximately 20 GPa, which is substantially lower than that of conventional titanium implants.

However, the mechanical environment of subcutaneous implants differs significantly from that of bone. Human skin is soft and flexible, but the exact skin properties vary with age, anatomical location and individual factors [49]. The mechanical properties varies depending on how the collagen fibres, cells and ground substance are organized. Skin tissue has a complex three-dimensional network of fibres, but the predominant fibre direction is parallel to the surface. Studies have determined that Young's modulus of skin typically ranges around 20 MPa, with variations depending on location, age and skin thickness [50], [51], [52].

Silicone are commonly used as a material in implants intended for contact with soft tissue, due to their elasticity, chemical stability, and low allergenic potential [53]. They are also heat-resistant and can thus be sterilized and stable for a long period of time. A significant stiffness mismatch between an implant and the surrounding tissue can lead to stress concentrations at the tissue–implant interface which may result in local irritation, inflammation, pressure-induced tissue damage, and patient discomfort. Materials with a low Young's modulus, such as silicone elastomers, better match the mechanical properties of soft tissue and deform more similarly to the surrounding tissue during movement. A silicone rubber provides an improved mechanical match compared to harder materials such as metals [54], [55]. This improved compliance reduces mechanical irritation and contributes to enhanced long-term tolerance of subcutaneous implants.

2.7.2 Materials currently used in Sentio

Sentio consists of, as mentioned previously, a bone-anchored transducer together with the antenna containing the receiver coils and permanent magnet.

Figure 2.10: Sentio. Image provided by Oticon Medical.

The permanent magnet currently used in the implant is a Sintered Samarium Cobalt magnet, also referred to as SmCo or Rare Earth magnet. The magnet is located in a casing made of a titanium alloy, namely Ti6Al4V Grade 5. The housing is in turn attached to the transducer by a reinforcement wire in titanium Grade 2. The wire is circular with a diameter of 0.6 mm and is welded in both ends. Its elastic modulus, or Young's modulus, is 105 GPa.

Around the magnet, there is a receiver coil in gold which picks up the signals from the external sound processor and transfers them to the transducer. The implant is overmolded by a liquid silicone rubber, with Shore 40A hardness.

2.8 Mechanical Properties of Silicone Elastomers

The mechanical properties of elastomers are often described using the Shore (durometer) hardness scale [56]. Different Shore scales exist depending on the stiffness of the material, such as Shore A and Shore D. The Shore A scale is typically used for softer elastomers and rubbers, while Shore D is used for harder elastomers and rigid polymers. The Shore hardness scale ranges from 0 to 100, where lower values correspond to softer materials and higher values indicate harder materials [57].

Although Shore hardness is not a direct measure of stiffness, it is related to the elastic modulus of elastomer materials. An approximate relationship between Shore A hardness and Young's modulus can be written as:

$$E = \frac{0.0981(56 + 7.66S)}{0.137505(254 - 2.54S)} \tag{2.4}$$

where E is the Young's modulus in MPa and S is the Shore A hardness [58].

Using this relationship, approximate Young's modulus values for different Shore A hardness levels can be estimated. The calculated values are shown in Table 2.1.

Table 2.1: Approximate relationship between Shore A hardness and Young's modulus for elastomers.

Shore A	Young's modulus (MPa)	Relative stiffness
20	∼0.7	∼0.4×
30	∼1.2	∼0.7×
40	∼1.7	1.0×
50	∼2.5	∼1.5×
60	∼3.6	∼2.1×
70	∼5.5	∼3.2×
80	∼9.3	∼5.5×
90	∼20.8	∼12.2x

As can be seen in Figure 2.11, the relationship is non-linear.

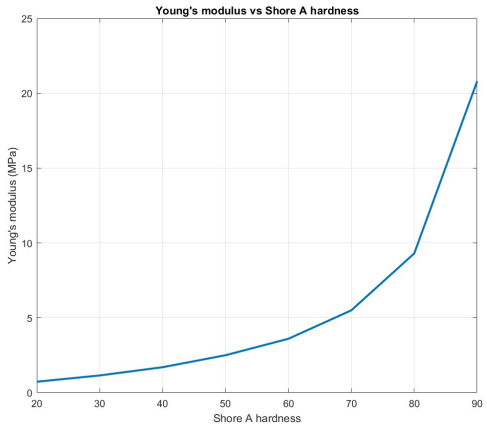

Figure 2.11: Relationship between Shore A and Young's modulus.

2.9 Euler-Bernoulli Beam Theory

The Euler-Bernoulli beam theory is a simple theory for describing how a beam deflects when it is exposed to a load [59]. It is a simplification of the linear theory of elasticity and thereby assumes that the material is linearly elastic. The theory also assumes that the cross-sectional area of the beam remains plane and normal to the deformed axis after deformation, and neglects any shear deformation or rotary inertia effects. It is mostly useful for long and slender beams and not applicable for short or thick beams. For this project, the reinforcement wire in Sentio is assumed to behave as a classic beam and to be slender enough to use Euler-Bernoulli beam theory.

According to Euler–Bernoulli beam theory, the relationship between bending moment and curvature is given by:

$$M(x) = EI\,\kappa(x), \qquad \kappa(x) \approx \frac{\mathrm{d}^2 w(x)}{\mathrm{d}x^2} \tag{2.5}$$

where $M(x)$ is the bending moment, E is Young's modulus, I is the second moment of area, and $\kappa(x)$ is the curvature of the beam [60]. The product EI is known as the flexural rigidity, or bending stiffness, and is a constant of the beam. If the wire is a circular wire, the cross-sectional area moment of inertia is defined as:

$$I_{circle} = \frac{\pi d^4}{64} \tag{2.6}$$

and the bending stiffness of a circular wire is therefore:

$$EI = E \cdot \frac{\pi d^4}{64} \tag{2.7}$$

This means that the bending stiffness EI is proportional to d^4, $EI \propto d^4$. Thus, if Young's modulus E is kept constant, the stiffness depends on the diameter of the wire only. If instead the diameter is kept constant, the stiffness depends only on Young's modulus.

However, for a wire with a square profile, the area moment of inertia becomes:

$$I_{square} = \frac{a^4}{12} \tag{2.8}$$

where a is the side-length of the square. Here, the bending stiffness EI is instead proportional to a^4 [61].

If the diameter of the circle equals the side of the square, $d = a$, the comparison between a circular wire and a square wire is as follows:

$$\frac{I_{square}}{I_{circle}} = \frac{a^4/12}{\pi d^4/64} = \frac{16}{3\pi} \approx 1.7 \tag{2.9}$$

Based on this theory, a square wire is 70% stiffer than a circular wire if the side-length and diameter is the same. The Euler-Bernoulli beam theory forms the basis for changing the parameters of the reinforcement wire properties in this project.

In reality, however, a square wire with sharp edges experiences more stress concentration at its corners compared to a circular wire [62]. This concentration of stress could cause the wire to experience locally higher tensions in the corners with a higher risk of crack initiation, and thereby a lower long-term stability compared to a circular wire.

2.10 Modelling in LS-DYNA

This project involves a model built in the Finite-Element method (FEM) solver LS-Dyna explicit R14.0.0.

2.10.1 Finite Element Method

The FEM is a numerical method used to solve differential equations that describe physical problems [63]. Instead of solving these equations for the entire model at once, the domain is divided into smaller parts called elements. Within each element, the unknown variables are approximated using simple functions. By combining all elements, the overall behaviour of the model can be described and solved using a system of equations.

LS-DYNA is a finite element solver developed at Livermore Software Technology Corporation and is maintained by Ansys [64]. It is widely used to analyse non-linear problems involving large deformations and complex interactions between materials.

In FEM, the elements are connected at nodes, where the unknown variables are calculated [65]. Different types of elements are used depending on the geometry [64]. Solid elements are typically used for thicker parts, while shell elements are used for thin structures.

A model is built by combining several parts that represent different components of the system being modelled [64]. Each part is assigned a material model and connected to other parts using contact definitions or constraints, allowing interaction during deformation. Loads and boundary conditions are applied to describe how the model is fixed and what forces or moments act on it, such as forces, displacements or moments applied to specific parts of the model. For materials that undergo large deformations, a non-linear analysis is required. This means that the deformation is not proportional to the applied load and can be caused by the material behaviour, geometry or contact.

2.10.2 Mooney-Rivlin Material Model

The Mooney-Rivlin material model is a common way in LS-Dyna to describe hyperelastic materials such as silicone or rubber [66]. Hyperelastic materials can stretch several hundred percent, and then return almost completely to the original shape. In LS-Dyna, this type of behaviour is based on strain energy density functions instead of linear stress-strain laws.

According to the Mooney-Rivlin model, the strain energy density W is defined as:

$$W = C_{10}(I_1 - 3) + C_{01}(I_2 - 3) \tag{2.10}$$

where W is the strain energy per unit volume, I_1 & I_2 are invariants of the deformation tensor and C_{10} & C_{01} are material constants that determine the stiffness of the rubber [67]. The parameters C_{10} and C_{01} are empirical values fitted from experiments. Higher values correspond to a stiffer material, while lower values result in a softer material.

For a silicone rubber, the Mooney-Rivlin parameters can be translated as:

$$E \approx 6(C_{10} + C_{01}) \tag{2.11}$$

where E is the elasticity modulus, or Young's modulus [68].

2.11 Magnetic Materials

In this section, different types of magnetic materials and their key properties are described.

2.11.1 Types of Magnetic Materials

Magnetic materials can be classified based on how they respond to an external magnetic field [69]. They can be divided into diamagnetic, paramagnetic, antiferromagnetic, ferrimagnetic, and ferromagnetic materials.

Diamagnetic and paramagnetic materials do not retain any magnetization in the absence of an external field [69]. Instead, they become weakly magnetized only when a field is applied. Diamagnetic materials develop a magnetization opposite to the applied field, resulting in a weak repulsion. Paramagnetic materials are magnetized in the same direction as the field, leading to a weak attraction.

Antiferromagnetic materials are characterized by magnetic moments that align antiparallel, resulting in no net magnetization [69]. Ferrimagnetic materials also exhibit opposing magnetic moments, but with unequal magnitudes, leading to a net magnetization. In contrast, ferromagnetic materials have magnetic moments that align parallel to each other, producing a strong net magnetization.

All materials have a magnetic permeability, μ. The relative permeability μ_r indicates how much induction is generated by the material in a given magnetic field [70]. Magnetic field lines prefer to travel in a material with high magnetic permeability. The magnetic permeability in vacuum is defined as $\mu_0 = 4\pi \cdot 10^{-7}$ H/m, and is typically used as a reference [71].

2.11.2 Magnetic Properties

The strength and orientation of a magnet can be described by its magnetic dipole moment m [72]. For a uniformly magnetized magnet, the magnetic moment can be described as:

$$m = MV, \qquad M = \frac{B_r}{\mu_0} \tag{2.12}$$

where m is the dipole moment, M is the magnetization, V is the volume, B_r is the remanent flux density and μ_0 is the magnetic permeability in vacuum.

The magnetic properties of ferromagnetic materials are often described using the hysteresis curve, which relates the magnetic flux density B to the applied magnetic

field H [72]. As shown in Figure 2.12, two important parameters are the remanent flux density B_r, which describes the remaining magnetization when the external field is removed and the coercive field H_c, which is the field required to reduce the magnetization to zero. These properties determine whether a material can retain magnetization and function as a permanent magnet.

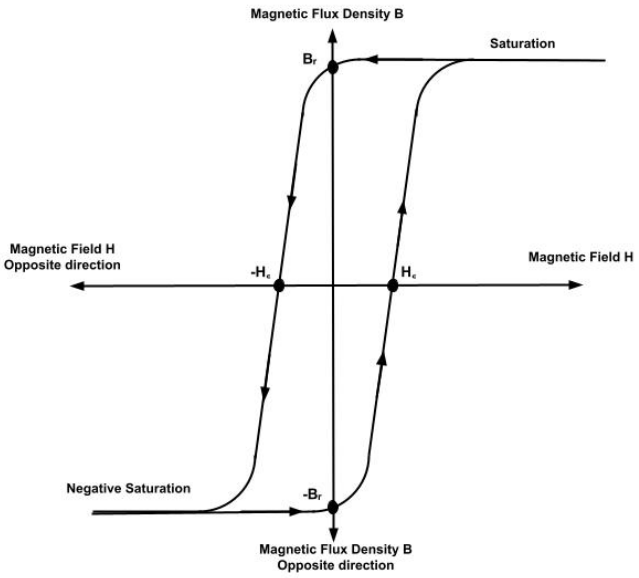

Figure 2.12: Hysteresis loop showing the remanent flux density B_r and the coercive field H_c. The upper and lower curves correspond to magnetization from positive and negative saturation.

The left side of the hysteresis loop describes how the material behaves when exposed to an opposing magnetic field and gradually becomes demagnetized [72]. If the applied field becomes large enough, partial or irreversible demagnetization may occur. Even without permanent demagnetization, the magnetization temporarily change when exposed to a strong external field, resulting in a reduced effective magnetic moment. Soft magnetic materials are characterized by low coercivity and can therefore be easily magnetized and demagnetized. Hard magnetic materials retain a significant magnetization due to their higher coercivity and are therefore suitable for use as permanent magnets.

In addition to its magnitude, magnetization also has a direction since it is a vector quantity [72]. In cylindrical permanent magnets, the magnetization is most commonly oriented either axially, along the cylinder axis or diametrically, across its diameter [73].

2.12 Pressure Pain Threshold

Pressure Pain Threshold (PPT) is used to determine the minimum pressure at which a sensation becomes painful in human tissue [74]. The method involves applying an increasing external pressure until the subject reports when the pressure changes

from no pain to minimally perceivable pain. PPT has in previous studies been measured in the temporalis muscle, which corresponds to the region where Sentio is placed, and is typically evaluated using algometers with a contact area of 50 mm^2 or 100 mm^2 [75], [76]. Reported in-vivo PPT values in this region when pressure is applied at the skin surface are approximately 282±70 kPa for adults [77].

3
Methods

A literature study was conducted including topics such as the auditory system, hearing loss, BC hearing devices, MRI compatibility of implants and relevant material properties. The information was critically evaluated and primarily based on scientific articles and documents provided by Oticon Medical. The methodology consisted of three main components.

The first part of the project included a computational approach to evaluate implant behaviour under MRI conditions, as it enables controlled variation of design parameters and detailed analysis of the mechanical response. The simulations focused on determining the displacement and pressure at 3T MRI compared with 1.5 T using the current design of the implant.

From this, potential design changes were identified which formed the basis of the second phase of the project. In this part of the study, the retention magnet was kept unchanged and the analysis therefore focused on the effect of the design of the reinforcement wire and the overmolded silicone.

The last part of the project focused on investigating alternative solutions for the retention magnet. The aim of this work was to explore possible design approaches that could improve MRI robustness while remaining feasible for use in a clinical implant system.

3.1 Baseline Simulation Model

The simulation work was based on the existing LS-DYNA model that had previously been used for evaluating Sentio at 1.5 T. Before starting the new simulations, the model files from the previous study were reviewed in order to understand the model and the simulation setup. Some initial simulations were also performed to gain an initial understanding of how the model behaves.

3.1.1 Simulation Model built in LS-DYNA

The simulations previously performed by FS Dynamics are used as a baseline for comparison. The model was built in LS-DYNA and is structured using multiple files defining elements and nodes, material models, boundary conditions, parts and

contact definitions. An overview of the simulation model and its main components is shown in Figure 3.1.

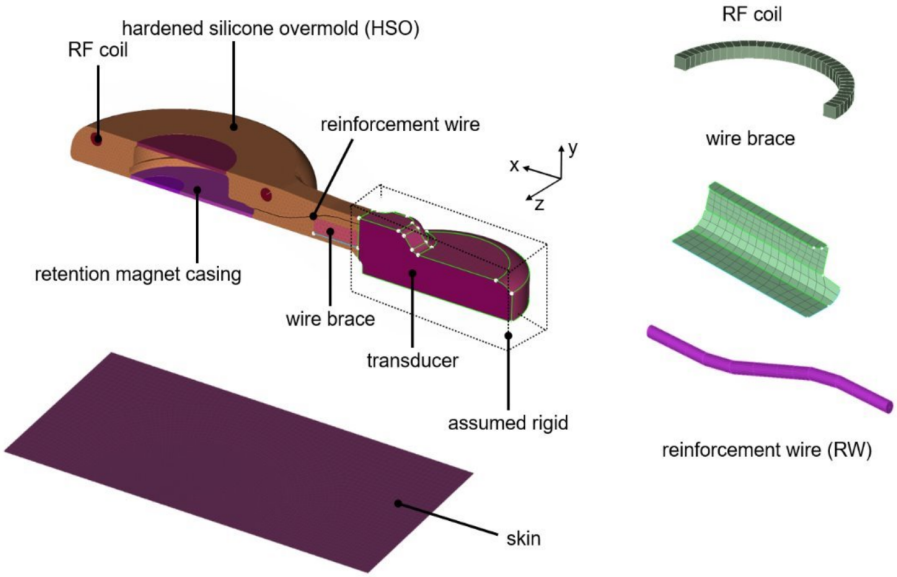

Figure 3.1: Overview of the simulation model including the implant and artificial skin. The corresponding material definitions are listed in Table 3.1. Image provided by Oticon Medical.

The corresponding material properties assigned to each component are listed in Table 3.1.

Table 3.1: Material properties used in the simulation. Note that the properties of titanium have been halved, since the model is a half symmetry model.
*Initial guess for Mooney-Rivlin parameters.

Part	**Material**	**Density** [kg/m^3]	**Stiffness** [GPa]	**Poisson's ratio**	**C10** [MPa]	**C01** [MPa]
RF coil	Gold	1932	77.2	0.42	-	-
Reinforcement wire (RW)	Titanium (grade 2)	2250	52.5	0.37	-	-
Wire brace	PEEK	1300	4	0.36	-	-
Artificial skin	Silicone Shore 60	1500	-	-	326.54*	112.4*
Overmolded silicone (HSO)	Shore 40	1500	-	-	104.74*	187.1*

The implant and the hardened silicone overmold (HSO) were modelled using ~ 0.3 mm large solid first-order tetrahedron elements, while the artificial skin was modelled using shell elements due to its small thickness. The reinforcement wire and coil were modelled using 1 mm long beam elements. The transducer attached to the bone and the magnet casing are assumed to be rigid, as they are significantly stiffer

than the surrounding components. Their deformation is therefore considered negligible. Since the implant is assumed to be completely symmetric, the model is set up as a half symmetry. The reinforcement wire is however built with full symmetry but instead the density and the stiffness (Young's modulus) is halved.

The mechanical behaviour of the silicone materials was described using a Mooney-Rivlin hyperelastic material model, see Equation 2.10, where the parameters C_{10} and C_{01} define the material response. Initially, both the artificial skin and the overmolded silicone were assigned estimated material parameters, as shown in Table 3.1.

The simulation model was calibrated using a two-step procedure based on data from physical bench tests. The artificial skin used in the simulation corresponds to the silicone layer used in the bench tests, modelled with $\sim$ 0.4 mm large shell elements with a thickness of 1 mm. In the bench tests, a force corresponding to the MRI-induced torque on the retention magnet was applied and the resulting displacement was measured. This displacement was used as a reference for calibrating and validating the simulation model. The calibration process is illustrated in Figure 3.2.

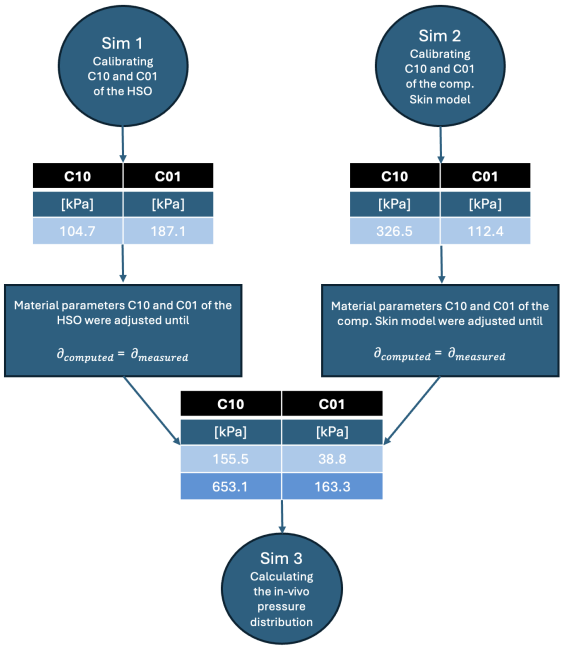

Figure 3.2: Overview of the calibration procedure based on experimental bench tests. The implant and artificial skin material parameters were calibrated sequentially and used in the final simulation. Image provided by Oticon Medical.

In the first step, the material parameters of the HSO were calibrated using results from the bench test performed without artificial skin. The experimentally measured displacement was compared to the simulation results and the material parameters were iteratively adjusted until the same displacement was achieved. A second bench test, including the artificial skin, was then used to calibrate the material parameters of the skin. Similarly, the simulated displacement was compared to the experimen-

tal results and the parameters were tuned iteratively. The final set of calibrated parameters was then used in the complete model.

Table 3.2 and 3.3 shows the final parameters of the overmolded silicone and the artificial skin, respectively. It should be noted that the calibrated parameters do not represent the actual material properties of the silicone, but are adjusted to match the behaviour observed in the experiments.

Table 3.2: Updated parameters of the overmolded silicone.

$\mathbf{C_{10}}$ **[kPa]**	$\mathbf{C_{01}}$ **[kPa]**
155.5	38.8

Table 3.3: Updated parameters of the artificial skin silicone.

$\mathbf{C_{10}}$ **[kPa]**	$\mathbf{C_{01}}$ **[kPa]**
653.08	163.27

Contact between components was defined so that the implant and surrounding materials can interact during deformation. Boundary conditions were applied to describe how the model is fixed and how it is allowed to move. Parts of the model were fixed to represent attachment to the skull and a predefined movement was applied to the skin.

To simulate the behaviour of the implant in a 1.5 T MRI, the experimentally obtained maximum torque of 366 mNm was applied on the center of gravity of the magnet with preloaded skin. This torque represents specifically how Sentio behaves in an external magnetic field of 1.5 T. Since half symmetry is used, a torque load of 183 mNm was used as input. The simulation was then solved step by step in time to handle the non-linear behaviour.

3.1.2 Outputs of Interest

The baseline simulation was used to evaluate the displacement of the implant at a torque of 1.5 T. This displacement was used as a reference for the simulations. The simulations aimed to identify parameter combinations that produced displacement comparable to the 1.5 T baseline.

The pressure on the artificial skin was evaluated by calculating the average pressure in two defined regions on the skin, referred to as region A and B, as shown in Figure 3.3. In both regions, the average pressure was calculated over areas of 25 mm^2 and 50 mm^2. These areas are based on reported PPT measurements (see Section 2.12), which are typically evaluated over contact areas of 50 mm^2 and 100 mm^2. However, due to the use of a half symmetry model, the evaluated areas correspond to 25 mm^2 and 50 mm^2 in the simulations. The pressure was not intended to be matched to

the baseline simulation, but rather compared between simulations, as it is related to the contact pressure experienced by the patient.

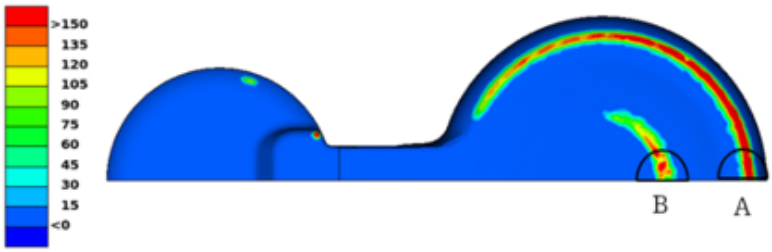

Figure 3.3: Pressure distribution on the device at 1.5 T, showing regions A and B.

3.2 Simulating Displacement and Pressure at 3 T

As the model takes torque as input, a new torque corresponding to a magnetic field strength of 3 T was estimated.

Based on Equation 2.3, the torque is proportional to the magnetic field strength for a fixed dipole moment and angle:

$$\tau \propto B \tag{3.1}$$

Thus, the torque scales linearly with the magnetic field strength. Consequently, increasing the magnetic field from 1.5 T to 3 T results in an approximate doubling of the torque:

$$\frac{\tau_{3T}}{\tau_{1.5T}} = \frac{B_{3T}}{B_{1.5T}} = \frac{3}{1.5} = 2 \tag{3.2}$$

Based on this relationship, the torque corresponding to a 3 T scenario was estimated to be 732 mNm. In the simulation, a torque of 366 mNm was applied since it uses half-symmetry.

To investigate potential design modifications for 3 T MRI conditions, the existing simulation model was updated using the new estimated torque for the 3 T case. Initially, the model was run with the updated torque without changing any other parameters in order to verify that the simulation converged. The resulting mechanical response was evaluated in terms of displacement and average pressure on the skin in regions A and B.

3.3 Simulation of Design Modifications

Changes to model parameters and simulation inputs were defined and provided to FS Dynamics, who implemented the changes in the LS-DYNA model and executed the

simulations. The results were then evaluated and used to guide further adjustments of selected parameters. The design changes investigated in this work mainly focused on the mechanical properties of the reinforcement wire and the overmolded silicone. Parameter fitting was performed manually by iteratively adjusting input values and comparing resulting displacement to the baseline.

3.3.1 Reinforcement Wire Properties

This section explains how the properties of the reinforcement wire were varied according to its stiffness, diameter dimensions and geometry.

3.3.1.1 Reinforcement Wire Stiffness

The stiffness of the reinforcement wire was investigated by modifying the Young's modulus of the material. As presented in section 2.9, the bending stiffness of the wire depends on both Young's modulus and the wire diameter according to Euler–Bernoulli beam theory.

To estimate a suitable starting point, the relative stiffness scaling was considered using:

$$\text{Stiffness factor} = \frac{E}{E_0}\left(\frac{d}{d_0}\right)^4 \tag{3.3}$$

where E and d are the Young's modulus and diameter of the wire, and E_0 and d_0 represent the original values in the baseline model.

Based on this relation, the first simulation was performed by doubling the Young's modulus of the reinforcement wire.
The results were then evaluated and the Young's modulus was further adjusted in order to try to obtain a similar mechanical response to the baseline simulation at 1.5 T.

3.3.1.2 Reinforcement Wire Diameter

The stiffness of the reinforcement wire was also investigated by changing the wire diameter. Using the same stiffness scaling relation as presented in section 2.9, the reinforcement wire stiffness was applied to estimate how changes in diameter would affect the overall stiffness.

Different wire diameters were evaluated relative to the baseline diameter of 0.6 mm. The estimated stiffness factors for the different diameters are shown in Table 3.4 below, when a titanium wire with Young's modulus of 105 GPa is used.

Table 3.4: Estimated stiffness scaling for different diameters of the reinforcement wire.

Diameter (mm)	**Stiffness factor**
0.60	1.00
0.65	1.36
0.70	1.85
0.72	2.07
0.75	2.44

Based on this estimation, a diameter of approximately 0.72–0.73 mm corresponds to roughly twice the bending stiffness of the original wire and was therefore used as the initial input for the simulations. The results were evaluated and diameter was further adjusted through parameter fitting in order to obtain the reference displacement.

3.3.1.3 Reinforcement Wire Geometry

The reinforcement wire has a circular geometry in the current design and was therefore previously modelled accordingly. To study the effect of changing the geometry, the wire was changed to a square profile.

A parametric study was performed where the side length of the square was varied using the same values as previously used for the circular wire diameter, in order to compare how the geometry influences the bending behaviour. For each case, simulations were carried out using the torque corresponding to a 3 T magnetic field to evaluate the resulting displacement. The side length was iteratively adjusted until a displacement corresponding to the reference case at 1.5 T was achieved.

3.3.2 Silicone Material Properties

The silicone in the model is described using a Mooney–Rivlin hyperelastic material model and is represented by the material parameters C_{10} and C_{01}. Since the material behaviour is defined through these parameters, it was not feasible to directly estimate which values would result in the desired change in stiffness.

As an initial step, the silicone stiffness was increased by scaling the existing material parameters by a factor of two. The simulation results were then evaluated and adjusted through iterative parameter fitting until the target displacement was reached. The goal was to obtain a mechanical response similar to the baseline simulation at 1.5 T in terms of displacement.

3.3.3 Combination of Design Parameters

Based on the prior results of silicone stiffness, reinforcement wire stiffness and wire diameter, an optimization step was performed focusing on silicone stiffness and wire

diameter.

The optimization was carried out by constructing a matrix of combinations of silicone stiffness and wire diameter based on values identified in earlier stages of this project, as shown in Table 3.5.

Table 3.5: Matrix used for parameter optimization.

	Silicone scale factor					
Diameter of wire (mm)	1	2	3	4	5	6
0.6						
0.7						
0.8						
0.9						
1.0		starting point				
1.1						
1.2						
1.3						
1.4						
1.5						
1.6						

The green cells represent configurations that were already tested in earlier steps, where only one parameter was varied at a time. Red cells were excluded, as they correspond to cases where the same displacement reduction had already been achieved by maximizing a single parameter. The yellow region represents an initial estimate of how the required parameter combinations could be distributed based on the selected starting point. This estimate followed a diagonal pattern in the matrix, under the assumption that a higher silicone stiffness would require a smaller wire diameter to achieve the same displacement.

A starting point of a 1.0 mm wire diameter and a silicone stiffness scaled by a factor of 2 was selected based on previous simulations of the parameters evaluated individually, where each of these values resulted in approximately a 25% reduction in displacement. This specific combination had not been tested prior to the optimization. From this point, simulations were performed by varying the parameters along the matrix. For each level of silicone stiffness, the wire diameter was adjusted until the target displacement corresponding to 1.5T (3.120 mm) was reached.

3.3.4 Implementation in Implant Design

After the simulation study, the resulting material parameters were evaluated to determine whether they correspond to realistic material properties. The different scaling factors of the silicone stiffness was translated into Shore Hardness according to the relative stiffness in Table 2.1 by using Equation 2.4. For the wire, the diameter was evaluated based on the limited space within the implant.

3.4 Investigation of Alternatives for the Retention System

The second part of the project focused on investigating alternative solutions through a concept generation process. The concepts were generated independently of existing commercial solutions to encourage design exploration and reduce bias.

The ideas were generated through a brainstorming process based on the magnetic torque, see equation 2.3. In an MRI system, the magnetic field strength B_0 is constant. Therefore, the design strategies focused on reducing the torque by reducing the contribution from the magnetic dipole moment m or from the angular term $\sin\theta$. The generated concepts were evaluated with respect to their feasibility in a clinical implant system. The evaluation focused on their influence on MRI-induced torque and retention between the internal and external component.

4

Results

4.1 Baseline Simulation Model

For completion, the results presented in this section were obtained from previous simulations following the generation and verification of the computer model (provided by Oticon Medical) when the current version of Sentio is subjected to 1.5 T.

Figure 4.1 illustrates the displacement of the implant during an MRI scan corresponding to 1.5 T. The displacement magnitude is shown by the color scale in millimeters, while the horizontal black line indicates the skull bone surface. The figure shows that the implant lifts from the skull bone surface due to the applied torque. The maximum displacement of the implant at 1.5 T was 3.12 mm.

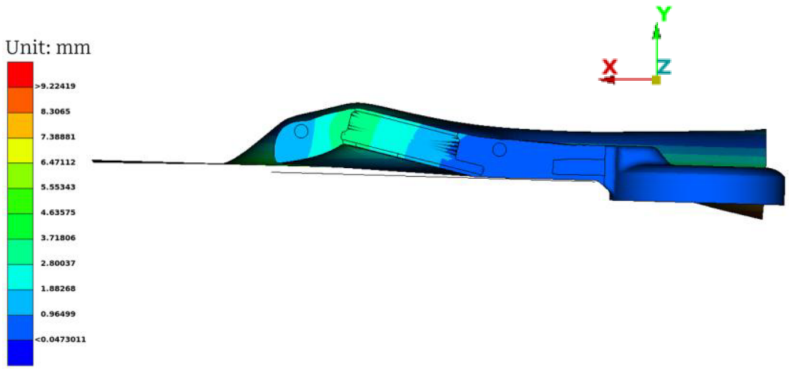

Figure 4.1: Total displacement of the implant at 1.5 T: 3.12 mm.

The average pressure on the artificial skin in regions A and B is presented in Table 4.1.

Table 4.1: Average pressure on the artificial skin in regions A and B for different evaluated areas at 1.5 T.

Area of region	Region B	Region A
25 mm^2	35 kPa	41 kPa
50 mm^2	24 kPa	32 kPa

4.2 Effect on Displacement and Pressure at 3 T

When subjected to 3 T the torque will double to 732 mNm, that is the worst case scenario without taking any partial demagnetization into account. Due to half symmetry in the model the torque applied in the simulation is therefore 366 mNm. When the new torque was applied to the model to see how the implant would behave in an MRI scan of 3 T, the displacement was compared to the 1.5 T baseline. The comparison of the displacement of the implant at 1.5 T is shown together with the results obtained for 3 T in Figure 4.2.

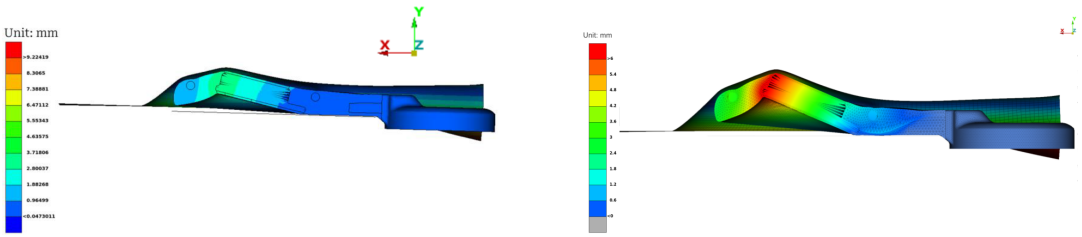

(a) Torque acting on magnet in 1.5 T MRI, resulting in 3.12 mm displacement.

(b) Torque acting on magnet in 3 T MRI, resulting in 5.65 mm displacement.

Figure 4.2: Displacement of implant in 1.5 T and 3 T MRI, resulting in 5.65 mm displacement.

At 3 T, the displacement increased from 3.12 mm to 5.65 mm, corresponding to an increase of approximately 81%.
Table 4.2 presents the average pressure on the skin in both regions at 1.5 T and at 3 T. The average pressure is higher in both region A and B for both areas compared to 1.5 T.

Table 4.2: Average pressure in regions A and B for 1.5 T and 3 T.

(a) 1.5 T

Area	Region B	Region A
25 mm^2	35 kPa	41 kPa
50 mm^2	24 kPa	32 kPa

(b) 3 T

Area	Region B	Region A
25 mm^2	98 kPa	76 kPa
50 mm^2	73 kPa	58 kPa

At 3 T, the average pressure increased by approximately 80–200% depending on region and area.

4.3 Effect of Design Modifications

Since the displacement and pressure on skin was significantly increased for the implant in 3 T, design modifications to the reinforcement wire and the overmolded silicone were investigated.

4.3.1 Effect of Reinforcement Wire Properties

The effect of varying the properties of the reinforcement wire according to its stiffness, diameter dimensions and geometry are presented in this section.

4.3.1.1 Effect of Reinforcement Wire Stiffness

Figure 4.3 shows how the displacement of the implant changes when changing the stiffness of the wire. When increasing the stiffness of the wire with a factor 4, there is only a limited reduction of the displacement to around 4.8 mm.

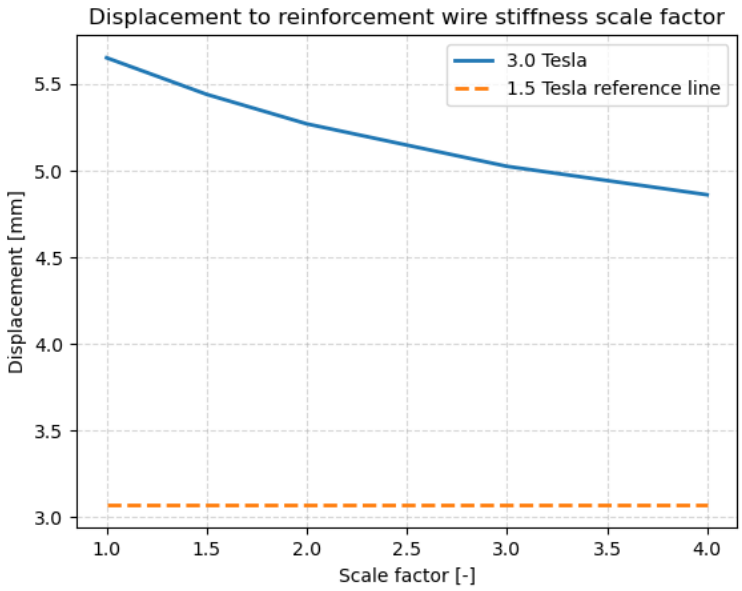

Figure 4.3: Influence of wire stiffness on displacement of implant.

Considering this, no further changes were made to the stiffness of the wire.

4.3.1.2 Effect of Reinforcement Wire Diameter

Approximately the same displacement as the current implant experiences in 1.5T is obtained when the diameter is increased to ∼1.56 mm compared to the original 0.6 mm, see Figure 4.4.

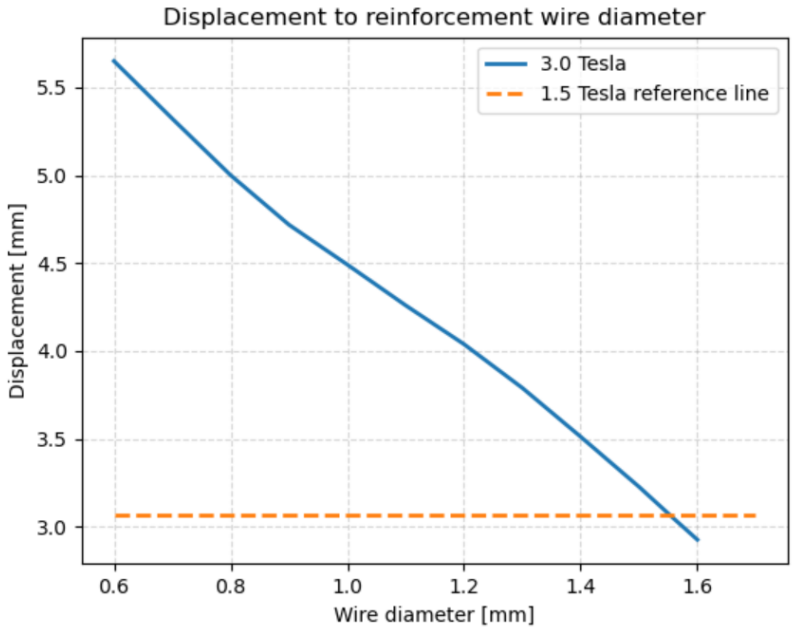

Figure 4.4: Effect of wire diameter on displacement.

Table 4.3 below presents the average pressure on the skin in both region at 1.5 T and at 3 T when the equal displacement is achieved, corresponding to a wire diameter of 1.56 mm. As can be seen in the table, the pressure is equal or lower for both evaluated areas and in both regions compared to 1.5 T.

Table 4.3: Average pressure in regions A and B at 1.5 T and at 3 T with a wire diameter of 1.56 mm.

(a) 1.5 T

Area	Region B	Region A
25 mm^2	35 kPa	41 kPa
50 mm^2	24 kPa	32 kPa

(b) 1.56 mm diameter

Area	Region B	Region A
25 mm^2	32 kPa	36 kPa
50 mm^2	24 kPa	28 kPa

4.3.1.3 Effect of Reinforcement Wire Geometry

In Figure 4.5, the displacement is shown as a function of the wire dimension for both circular and square profiles at 3 T.

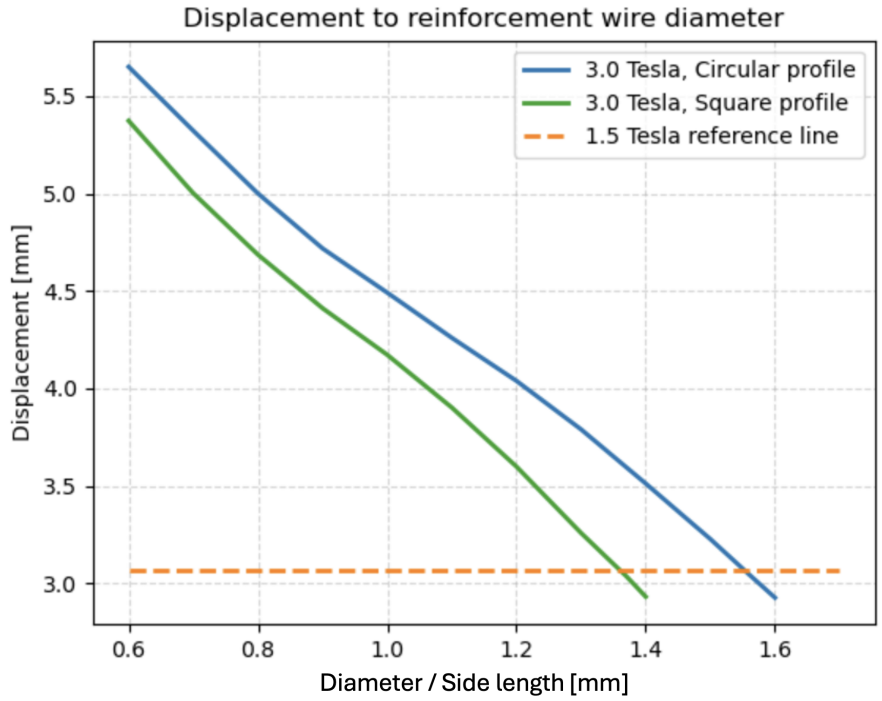

Figure 4.5: Displacement as a function of wire dimension for circular and square profiles at 3 T, compared to 1.5 T.

For both cases, the displacement decreases as the wire dimension increases. The square profile gives a lower displacement than the circular profile when the diameter of the circle is the same as the side length of the square. The reference displacement at 1.5 T is reached at a wire dimension of approximately 1.37 mm for the square profile, compared to 1.56 mm for the circular wire.

In Table 4.4, the average pressure on the skin in both regions is presented for the circular and square wire geometries at dimensions corresponding to the reference displacement. The square profile generally results in slightly higher pressure values compared to the circular profile, except for region B at 25 mm^2 where the pressure is slightly lower. Overall, the differences between the two geometries are small.

Table 4.4: Average pressure on the skin in regions A and B for circular and square wire geometries at dimensions that generates equal displacement as the reference.

(a) Circle: 1.56 mm diameter

Area	Region B	Region A
25 mm^2	32 kPa	36 kPa
50 mm^2	24 kPa	28 kPa

(b) Square: 1.37 mm side length

Area	Region B	Region A
25 mm^2	32 kPa	36 kPa
50 mm^2	23 kPa	29 kPa

4.3.2 Effect of Silicone Material Properties

As can be seen in figure 4.6, scaling the silicone parameters with 6.25 gives approximately the same displacement of the implant as the current implant experiences in 1.5 T.

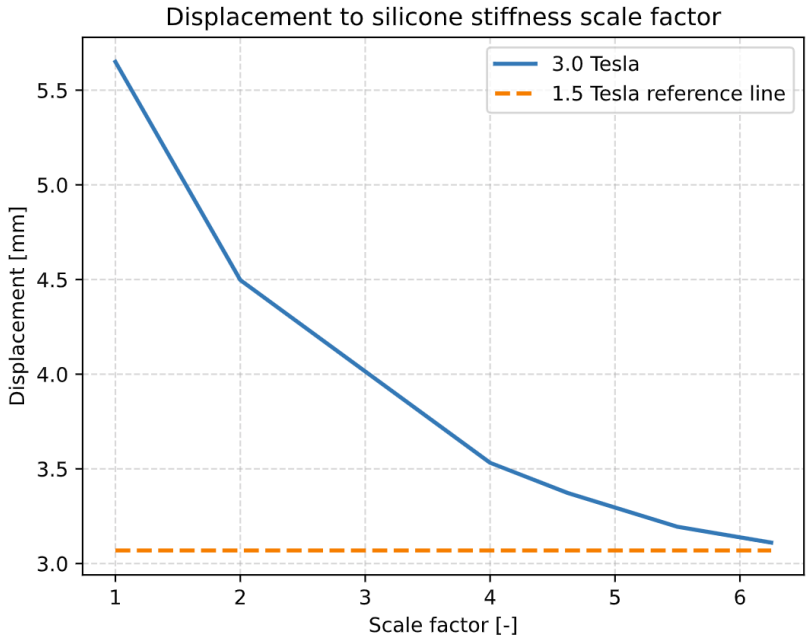

Figure 4.6: Displacement of implant depending on scale factor of silicone parameters C_{10} & C_{01}.

Table 4.5 below presents the average pressure on the skin in both regions at 1.5 T and at 3 T when the same displacement is achieved, corresponding to a 6.25× increase in silicone stiffness. As can be seen in the table, the pressure is higher in region A for both areas compared to 1.5 T, while it is lower in region B.

Table 4.5: Average pressure in regions A and B for 1.5 T and 6.25× silicone stiffness at 3 T.

(a) 1.5 T

Area	Region B	Region A
25 mm^2	35 kPa	41 kPa
50 mm^2	24 kPa	32 kPa

(b) 6.25x

Area	Region B	Region A
25 mm^2	16 kPa	106 kPa
50 mm^2	10 kPa	81 kPa

4.3.3 Effect of Combinations of Design Parameters

Table 4.6 shows the displacement in mm of the implant in 3 T for various combinations of silicone stiffness and wire diameter, used as comparison for the reference displacement of 3.12 mm. The combinations that results in the equal or lower displacement are marked with red circles in the table.

	Silicone scale factor					
Diameter of wire (mm)	1	2	3	4	5	6
0.6						
0.7				3,358	3,132	
0.8			3,51	3,21	2,993	
0.9		3,779	3,303	3,055		
1.0		3,593	3,114			
1.1		3,378	2,955			
1.2		3,2				
1.3		3,023				
1.4						
1.5						
1.6						

Table 4.6: Optimization of silicone stiffness and wire diameter. Green area: already tested, red area: rejected values.

In addition to the previous cases when focusing only on either the silicone or the wire thickness, four parameter combinations achieved displacement equal to or lower than the 1.5 T reference:

- Case 1: 2x stiffer silicone + 1.3 mm wire diameter
- Case 2: 3x stiffer silicone + 1.0 mm wire diameter
- Case 3: 4x stiffer silicone + 0.9 mm wire diameter
- Case 4: 5x stiffer silicone + 0.7 mm wire diameter

Table 4.7 below presents the average pressure on the skin in both regions at 3 T for different combinations of silicone stiffness and wire diameter that achieve the reference displacement. The pressure is higher in region A for all cases compared to the reference, while it is lower in region B.

Table 4.7: Average pressure in regions A and B for different combinations of silicone stiffness and wire diameter at 3 T, achieving the reference displacement.

Case	**Silicone**	**Wire**	**25 mm^2**		**50 mm^2**	
			B (kPa)	**A (kPa)**	**B (kPa)**	**A (kPa)**
Ref. (1.5 T)	1x	0.6 mm	35	41	24	32
Case 1	2x	1.3 mm	26	60	18	46
Case 2	3x	1.0 mm	23	80	16	60
Case 3	4x	0.9 mm	19	89	13	68
Case 4	5x	0.7 mm	18	100	12	76

4.3.4 Implementation in Implant Design

When translating the scaling of silicone stiffness into Shore A hardness according to Table 2.1 and Equation 2.4, the following results were obtained:

Table 4.8: Estimated stiffness scaling for different diameters of the reinforcement wire.

Case	Scale factor	Shore A hardness
Case 1	2x	60A
Case 2	3x	70A
Case 3	4x	75A
Case 4	5x	80A
Only changing silicone	6.25x	85A

Figure 4.7 shows the implant with its original wire diameter of 0.6 mm next to when the wire has a diameter of 1.56 mm. The wire is welded into the titanium casing of both the transducer and the retention magnet. More images of the implant with different wire diameters can be found in Appendix.

(a) 0.6 mm wire diameter, cross-sectional view

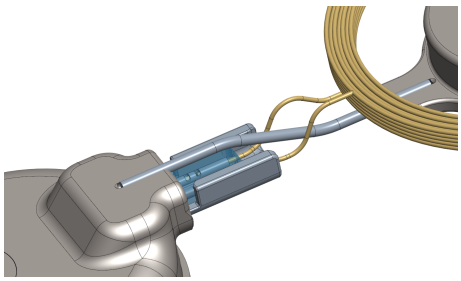

(b) 0.6 mm wire diameter in implant

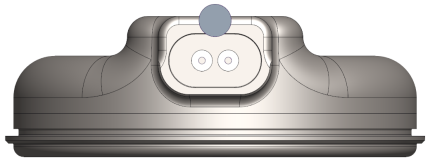

(c) 1.56 mm wire diameter, cross-sectional view

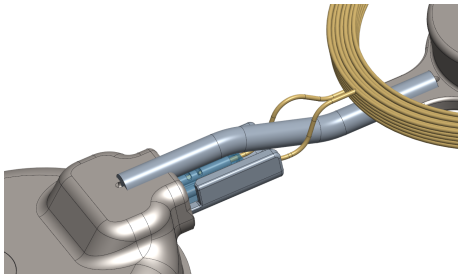

(d) 1.56 mm wire diameter in implant

Figure 4.7: Effect of increasing diameter of wire in implant to 1.56 mm. Images provided by Oticon Medical.

4.4 Investigation of Alternatives for the Retention System

There are various ways to reduce the torque that a magnet experiences in an external magnetic field. The induced torque can be reduced by minimizing the magnetic dipole moment or the angular contribution. Based on this, a mindmap of the initial ideas was created, see Figure 4.8. Additional ideas were also explored along the way.

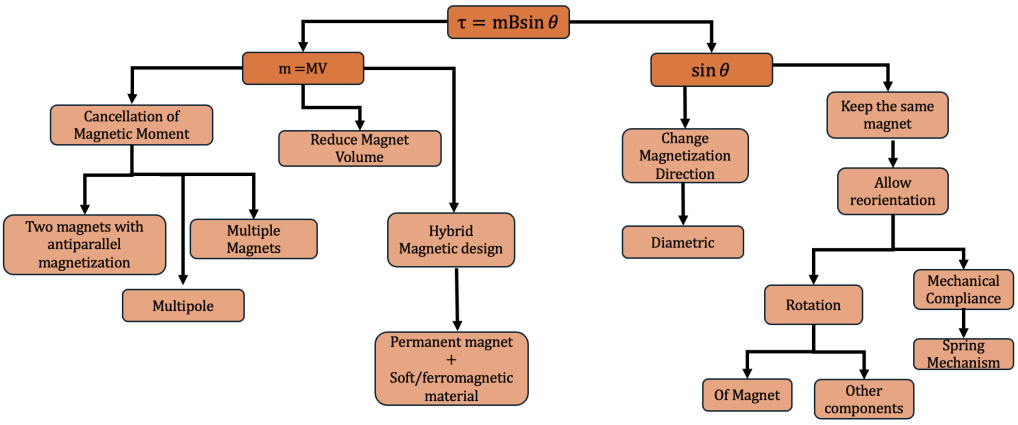

Figure 4.8: Mindmap used for concept generation based on the magnetic torque equation.

The magnetic dipole moment can be reduced by using two magnets with anti-parallel magnetization, multiple magnets or magnets with a multipole configuration. In this case, the resulting magnetic moment is partially cancelled out due to the opposite magnetization directions. The magnet volume can be adjusted in order to reduce the magnetic torque, since a smaller magnet results in a lower magnetic moment. However, the magnet must still be large enough to provide sufficient retention, which limits how much the volume can be reduced. At the same time, the magnet should not occupy too much space within the implant, meaning that there are both lower and upper constraints on the size. Another option is to replace the permanent magnet in the implant with a ferromagnetic material. However, the main limitation is reduced retention. Compared to two permanent magnets, the magnetic coupling is significantly weaker.

The angular contribution can be reduced by either changing the direction of magnetization, or allowing movement or rotation of the magnet to enable alignment with the external magnetic field. Using a mechanical solution is considered the most promising idea since it reduces magnetic torque independently of the orientation of the implant. Furthermore, a single permanent magnet can be used which would give the maximum retention force towards the external sound processor.

Changing the magnetization direction can influence the resulting torque. However, as long as the magnet cannot align with the external field, the worst-case torque will

still be large. For example, a diametrically magnetized magnet could in one direction be aligned with the field, but in the other it will be affected by the field until it reaches the worst-case angle (90°). Since worst-case should always be evaluated, it is not sufficient to have a solution that is optimized for one specific angle in MRI.

Based on the initial ideas in the mindmap, solutions were defined and evaluated in detail, regarding both retention force and induced magnetic torque. However, this part is not disclosed in this report due to intellectual property reasons, as requested by Oticon Medical.

5
Discussion

This chapter discusses the results of the study, including the effect of 3 T MRI, design modifications, alternative retention systems and future work.

5.1 Effect on Displacement and Pressure at 3 T

In this project, the MRI compliance of Sentio has been evaluated based on the worst-case induced magnetic torque. In reality, this torque is likely lower. It was assumed that the permanent magnet is not fully demagnetized at 3 T, but partial demagnetization may occur, reducing the effective magnetic moment. This suggests that the torque used in this study is likely overestimated and should be verified by physical testing.

When applying the estimated torque of 366 mNm (due to half symmetry), the displacement increased from 3.12 mm at 1.5 T to 5.65 mm at 3 T. The non-linear material behaviour of the silicone likely explains why the displacement is not exactly doubled, as the material becomes stiffer at larger deformations. However, the simulated displacement may not fully represent reality, as the model uses a simplified 1 mm silicone layer instead of real human skin.

The pressure on the skin also increases significantly at 3 T. At 3 T, both the displacement and contact pressure on skin increased substantially, with pressure rising by approximately a factor of 2 in region A and 3 in region B. In the baseline case, the maximum pressure occurs at the outer edge of the implant (region A), while at 3 T it shifts towards the magnet (region B). This indicates that design modifications are required for the implant to be compatible with 3 T MRI.

5.2 Effect of Design Modifications

The simulations showed that the diameter of the reinforcement wire has the greatest influence on both displacement and pressure on the skin. Increasing the diameter to 1.56 mm reduced the average pressure in both region A and B. This agrees with beam theory, where a larger diameter increases bending stiffness and reduces deformation. The Euler-Bernoulli beam theory was used to estimate initial values for the wire properties, but it did not accurately predict the displacement. This is likely due to the implant being a complex system with multiple interacting components, making the beam theory too simplified. However, it was still useful in indicating

that the wire diameter has a greater impact on the mechanical response than the Young's modulus.

When varying the stiffness of the reinforcement wire while keeping the diameter at 0.6 mm, only a small reduction in displacement was observed. Due to its thin and bent geometry, the wire remains flexible regardless of material stiffness. Even when increasing the Young's modulus by a factor of four, the displacement was only reduced by approximately 0.85 mm. Titanium was kept as the wire material due to its biocompatibility and non-magnetic properties, and the focus was instead on modifying the diameter and geometry. However, the combined effect of increasing both the Young's modulus and the diameter was not investigated and may have a greater impact. In addition, only titanium Grade 2 was considered, and it remains unclear how alternative materials, such as titanium Grade 5, would affect the results.

A square cross-section was tested to evaluate the effect of geometry on the mechanical response. When the side length was equal to the diameter of the circular wire, the square resulted in a slightly lower displacement, while the pressure remained almost unchanged. This is likely due to the larger cross-sectional area rather than the shape itself. However, the square profile is not considered suitable, as stress concentrations may occur in the corners, making the circular wire a more durable option.

When increasing the silicone stiffness while keeping the original reinforcement wire, the pressure in region B decreased while the pressure in region A increased. A stiffness 6.25 times higher was required to match the displacement at 1.5 T. However, this resulted in a pressure increase of approximately 2.5 times in region A and a decrease of around 2 times in region B. This indicates that the increased silicone stiffness reduces local deformation around the magnet, resulting in a more rigid-body-like motion of the implant.

A silicone stiffness 6.25 times higher corresponds approximately to Shore 85A, which may not be feasible for an implant as it behaves more like a hard plastic. Increasing the wire diameter to 1.56 mm is another way to achieve the desired response. However, there is limited space within the implant and the bigger wire diameter would require design changes in both the titanium casings and the thickness of the overmolded silicone. The combined cases, where both wire diameter and silicone stiffness are modified, are therefore more feasible. In these cases, the implant becomes less deformable, leading to increased pressure in region A and decreased pressure in region B. Among these, case 2, with a 1 mm wire and silicone corresponding to Shore 70A, appears to be the most realistic option, although it still results in higher pressure in region A.

In this study, the focus was on matching the displacement to the baseline case. However, pressure may be a more relevant measure, as it better represents what is experienced by the patient. It may therefore not be necessary to strictly match the displacement, as long as the pressure remains acceptable. Since a wire diameter of

1.56 mm results in equal or lower average pressure in both regions, it may be possible to use a slightly smaller diameter. This would likely increase the displacement somewhat, but could still provide an acceptable pressure distribution.

The computer model used in this study has previously been validated against physical bench tests, which supports the reliability of the simulation results. However, due to the non-linear behaviour of the silicone, it is uncertain how accurately changes in stiffness are represented. The silicone in the current implant (Shore 40A) is modelled using the Mooney-Rivlin parameters C10 and C01 (Table 3.2). When these are translated to a Young's modulus using Equation 2.11, the result is approximately 1.2 MPa, which does not directly correspond to Shore 40A values in Table 2.1. This is likely because the model has been calibrated to reproduce the overall implant behaviour rather than the material properties alone. Therefore, the silicone stiffness in this study was interpreted in a relative sense using equation 2.4, assuming that scaling the Mooney-Rivlin parameters corresponds to a proportional change in stiffness.

5.3 Alternatives for the Retention System

Reducing the magnetic induced torque while remaining the same magnetic retention force is physically contradictory and has been the main issue of this part of the project. A sufficiently strong magnet is required to attract the external sound processor through skin tissue of various thicknesses.

This suggests that a permanent magnet is the best option to remain as high as possible retention. Therefore, the ideas regarding using two anti-parallel, allowing rotation or movement of the magnet are considered the most promising solutions. Furthermore, this project has been limited to focus on magnetically induced torque only. The mentioned concepts may introduce additional problems to the implant in terms of size or manufacturing. In addition, some ideas may introduce other incompatibilities with MRI such as heating or exposure to translational forces.

If the current implant design is maintained, a magnet that can align with the external magnetic field, such as the concepts involving a rotating magnet, is likely the most feasible solution.

Alternatively, modifications to the retention system could be combined with design changes to the implant. Increasing the wire diameter and slightly stiffening the silicone has been shown to reduce displacement, although it may increase pressure in certain regions. In this case, a magnet that allows some movement, could help reduce the pressure without requiring full alignment.

5.4 Future Work

Future work should focus on experimental validation of the simulated torque and displacement under 3 T MRI conditions. Although this study evaluates feasible material changes, it remains uncertain whether the proposed designs provide sufficient flexibility to fit different skull anatomies or can be implemented in a transcutaneous implant.

A limitation of this study is that only the silicone and reinforcement wire properties were investigated. Other components, such as the size and shape of the silicone that surrounds the reinforcement wire, the wire brace, and the magnet casing, were not considered and may influence the overall behaviour. Future studies could therefore explore additional design changes, for example increasing the silicone stiffness only around the magnet to reduce deformation while maintaining overall flexibility.

In addition, the reinforcement wire could be further optimized. Since space within the implant varies, an asymmetrical wire design could be investigated, where the diameter is increased in regions prone to bending. However, this may introduce stress concentrations and would need to be evaluated.

The concepts for alternative retention magnet systems are based on initial concept generation and have not been experimentally verified. Further work is therefore required to evaluate their feasibility, including retention force and long-term performance in a medical implant.

6
Conclusion

This project has evaluated how Sentio behaves when subjected to a magnetic torque corresponding to a 3 T MRI environment. The results show that both displacement and pressure increase significantly compared to 1.5 T, with displacement close to doubled and pressure on skin increasing by a factor of approximately 2–3. This means that the current design does not meet the requirement of maintaining the same mechanical response at 3 T, and design changes are therefore needed.

The reinforcement wire was found to have the greatest influence on both displacement and pressure. Increasing the wire diameter is the only modification that reduces both, but the required size of 1.56 mm is likely not feasible within the current design of the implant. Changing the silicone stiffness alone is not suitable, as it leads to an increased pressure distribution. A more realistic approach is to combine moderate changes in wire diameter and silicone stiffness, where a 1 mm wire together with a Shore 70A silicone provides a reasonable compromise, although it does not fully match the pressure in the 1.5 T case.

One possible approach is to keep the current retention system and instead continue optimizing the design. For example, case 2 could be used as a starting point and then the pressure could be reduced further by investigating additional design parameters such as local changes in silicone stiffness or reinforcement wire geometry. Another approach is to keep the current design and instead only modify the magnet, where a permanent magnet that can rotate and align with the external magnetic field is considered promising. A third approach is to combine moderate design changes with the ideas regarding a magnet that allows some movement within its casing. This does not allow full alignment to the magnetic field but still reduces the induced torque and thereby pressure on skin.

In conclusion, modifying only the implant structure based on the parameters investigated in this study does not fully match the 1.5 T case, as case 2 achieves the same displacement but still results in a somewhat higher pressure. However, the relatively small difference suggests that the design is close to meeting the requirements. This indicates that further optimization of additional design parameters may be sufficient to achieve acceptable pressure levels, without necessarily modifying the retention magnet system. However, if the current flexible design of the implant is to be preserved, the retention magnet should be modified.

Bibliography

[1] *Deafness and hearing loss*, en, publisher: World Health Organization, Feb. 2025. Accessed: Feb. 12, 2026. [Online]. Available: https://www.who.int/news-room/fact-sheets/detail/deafness-and-hearing-loss.

[2] P. Van De Heyning et al., "Two-phase survey on the frequency of use and safety of MRI for hearing implant recipients," en, *European Archives of Oto-Rhino-Laryngology*, vol. 278, no. 11, pp. 4225–4233, Nov. 2021, ISSN: 0937-4477, 1434-4726. DOI: 10.1007/s00405-020-06525-3. Accessed: Feb. 12, 2026. [Online]. Available: https://link.springer.com/10.1007/s00405-020-06525-3.

[3] U.S. Food and Drug Administration, "510(k) premarket notification clearance for sentio ti implant kit; sentio 1 mini; genie medical bahs," U.S. Food and Drug Administration, Silver Spring, MD, USA, Tech. Rep. K240614, Jul. 2024.

[4] Y. A. Al-Naser and D. Tafti, "MRI Patient Safety And Care," eng, in *StatPearls*, Treasure Island (FL): StatPearls Publishing, 2025. Accessed: Jan. 28, 2026. [Online]. Available: http://www.ncbi.nlm.nih.gov/books/NBK604477/.

[5] J. Alvarez-Linera, "3T MRI: Advances in brain imaging," eng, *European Journal of Radiology*, vol. 67, no. 3, pp. 415–426, Sep. 2008, ISSN: 0720-048X. DOI: 10.1016/j.ejrad.2008.02.045.

[6] J. O. Pickles, *An Introduction to the Physiology of Hearing*, 4th ed. Leiden, The Netherlands: Brill, 2012.

[7] National Institutes of Health, *Ear illustration*, https://commons.wikimedia.org/wiki/File:Ear_illustration.jpg, Public domain. Accessed: 2026-04-29, 2022.

[8] C. Elberling and K. Worsoe, *Fading Sounds: About Hearing and Hearing Aids*. The Oticon Foundation, 2006.

[9] M. Ugarteburu, R. H. Withnell, L. Cardoso, A. Carriero, and C.-P. Richter, "Mammalian middle ear mechanics: A review," *Frontiers in Bioengineering and Biotechnology*, vol. 10, p. 983 510, Oct. 2022, ISSN: 2296-4185. DOI: 10.3389/fbioe.2022.983510. Accessed: Feb. 4, 2026. [Online]. Available: https://www.ncbi.nlm.nih.gov/pmc/articles/PMC9589510/.

[10] S. Reinfeldt, S. Stenfelt, T. Good, and B. Håkansson, "Examination of bone-conducted transmission from sound field excitation measured by thresholds, ear-canal sound pressure, and skull vibrations," eng, *The Journal of the Acoustical Society of America*, vol. 121, no. 3, pp. 1576–1587, Mar. 2007, ISSN: 0001-4966. DOI: 10.1121/1.2434762.

[11] M. Eeg-Olofsson, *Transmission of bone-conducted sound in the human skull based on vibration and perceptual measures*. Göteborg : [Västra Frölunda]: Department of Otorhinolaryngology, Institute of Clinical Sciences, The Sahlgren-

ska Academy at the University of Gothenburg ; [Eeg-Olofsson, Måns], 2012, ISBN: 9789162884307.

[12] M. Zhao, A. Fridberger, and S. Stenfelt, "Vibration direction sensitivity of the cochlea with bone conduction stimulation in guinea pigs," *Scientific Reports*, vol. 11, p. 2855, Feb. 2021, ISSN: 2045-2322. DOI: 10.1038/s41598-021-82268-3. Accessed: Feb. 4, 2026. [Online]. Available: https://www.ncbi.nlm.nih.gov/pmc/articles/PMC7858597/.

[13] K.-J. Fredén Jansson, *The balanced electromagnetic separation transducer for bone conduction audiometry and hearing rehabilitation*. Göteborg: Chalmers University of Technology, 2017, ISBN: 9789175975689.

[14] M. Yonemura, *Why do recordings of one's own voice sound so strange?* en. Accessed: Feb. 4, 2026. [Online]. Available: https://www.u-tokyo.ac.jp/focus/en/features/z1304_00237.html.

[15] CDC, *Types of Hearing Loss*, en-us, May 2024. Accessed: Feb. 4, 2026. [Online]. Available: https://www.cdc.gov/hearing-loss-children/about/types-of-hearing-loss.html.

[16] D. Clason and E. Ostrowski, "Causes of sensorineural hearing loss (SNHL)," Healthy Hearing, Tech. Rep., Jun. 2025. Accessed: Feb. 4, 2026. [Online]. Available: https://www.healthyhearing.com/report/50276-Common-causes-of-sensorineural-hearing-loss.

[17] *Conductive Hearing Loss*, en-AU, Apr. 2022. Accessed: Feb. 5, 2026. [Online]. Available: https://www.earscience.org.au/2022/04/06/conductive-hearing-loss-symptoms-and-treatments/.

[18] R. Winters and C. Shermetaro, "External Ear Aural Atresia," eng, in *StatPearls*, Treasure Island (FL): StatPearls Publishing, 2025. Accessed: Feb. 5, 2026. [Online]. Available: http://www.ncbi.nlm.nih.gov/books/NBK563257/.

[19] *Conductive Hearing Loss: Symptoms, Causes, Diagnosis & Treatment - Tender Palm Super Speciality Hospital Lucknow, India*. Accessed: Feb. 5, 2026. [Online]. Available: https://www.tenderpalm.com/conductive-hearing-loss-treatment-in-lucknow-india#:~:text=Among%20children%2C%20the%20most%20common,ear%20injury%20or%20health%20condition.'.

[20] E. Ostrowski, "Types of hearing loss," *Healthy Hearing*, May 2025. Accessed: Feb. 4, 2026. [Online]. Available: https://www.healthyhearing.com/help/hearing-loss/types.

[21] L. James, *Mixed hearing loss*, en-US, Jan. 2025. Accessed: Feb. 5, 2026. [Online]. Available: https://www.thcp.co.uk/articles/mixed-hearing-loss.

[22] A. Pantaleo, A. Murri, G. Cavallaro, V. Pontillo, D. Auricchio, and N. Quaranta, "Single-Sided Deafness and Hearing Rehabilitation Modalities: Contralateral Routing of Signal Devices, Bone Conduction Devices, and Cochlear Implants," en, *Brain Sciences*, vol. 14, no. 1, p. 99, Jan. 2024, ISSN: 2076-3425. DOI: 10.3390/brainsci14010099. Accessed: Feb. 5, 2026. [Online]. Available: https://www.mdpi.com/2076-3425/14/1/99.

[23] *Air Conduction Hearing Aid - an overview | ScienceDirect Topics*. Accessed: Feb. 4, 2026. [Online]. Available: https://www.sciencedirect.com/topics/nursing-and-health-professions/air-conduction-hearing-aid.

[24] S. E. Ellsperman, E. M. Nairn, and E. Z. Stucken, "Review of Bone Conduction Hearing Devices," *Audiology Research*, vol. 11, no. 2, pp. 207–219, May 2021, ISSN: 2039-4330. DOI: 10.3390/audiolres11020019. Accessed: Feb. 4, 2026. [Online]. Available: https://www.ncbi.nlm.nih.gov/pmc/articles/PMC8161441/.

[25] S. Reinfeldt, B. Håkansson, et al., "New developments in bone-conduction hearing implants: A review," *Medical Devices: Evidence and Research*, 2015, Discusses static pressure requirements and soft tissue attenuation in early bone conduction devices. [Online]. Available: https://www.ncbi.nlm.nih.gov/pmc/articles/PMC4303401/.

[26] C. V. M. Verhagen, M. K. S. Hol, W. Coppens-Schellekens, A. F. M. Snik, and C. W. R. J. Cremers, "The Baha Softband: A new treatment for young children with bilateral congenital aural atresia," *International Journal of Pediatric Otorhinolaryngology*, vol. 72, no. 10, pp. 1455–1459, Oct. 2008, ISSN: 0165-5876. DOI: 10.1016/j.ijporl.2008.06.009. Accessed: Feb. 4, 2026. [Online]. Available: https://www.sciencedirect.com/science/article/pii/S0165587608002644.

[27] *Cochlear™ Osia Hearing Implant*, en. Accessed: Feb. 16, 2026. [Online]. Available: https://www.cochlear.com/us/en/home/products-and-accessories/cochlear-osia-system/osia-implants.

[28] *Cochlear™ Osia® System becomes industry's first active bone conduction system to enable MRI at 3 Tesla*, en. Accessed: Apr. 20, 2026. [Online]. Available: https://www.cochlear.com/us/en/corporate/media-center/media-releases/2023/osia-system-becomes-industrys-first-active-bone-conduction-system-to-enable-mri-at-3-tesla.

[29] *BCI 602 Bone Conduction Implant | MED-EL Pro*, en. Accessed: Feb. 17, 2026. [Online]. Available: https://www.medel.pro/hearing-solutions/bc/bonebridge/bci602.

[30] *Sentio System*, Oticon Medical. Accessed: Feb. 16, 2026. [Online]. Available: https://sentio.oticonmedical.com/.

[31] *Sentio Candidacy Guide*, Oticon Medical. Accessed: Feb. 16, 2026. [Online]. Available: https://p3.aprimocdn.net/dgs/ee8acc7b-d591-4e4a-b63b-b19200d94823/275106en_GUIDE_Sentio%20Candidacy%20Guide_Version%20B_2024.07_Original%20file.pdf.

[32] *Sentio Ti Implant Kit - Instructions for Use*, Oticon Medical. Accessed: Feb. 16, 2026. [Online]. Available: https://www.oticonmedical.com/downloads/?filters=84568b18e9234f078a5089adb3611364.

[33] G. Katti, S. A. Ara, and A. Shireen, "Magnetic Resonance Imaging (MRI) - A Review," *International Journal of Dental Clinics*, Dec. 2010, ISSN: 09758437.

[34] R. Ansorge and M. Graves, *The Physics and Mathematics of MRI*. Morgan & Claypool Publishers, 2016.

[35] J. Ainali, *Philips mri scanner at sahlgrenska university hospital*, https://commons.wikimedia.org/wiki/File:MRI-Philips.JPG, CC BY 3.0. Accessed: 2026-04-29.

[36] M. A. Bernstein, J. H. III, and H. A. Ward, "Imaging artifacts at 3.0t," *Journal of Magnetic Resonance Imaging*, vol. 24, no. 4, pp. 735–746, 2006. DOI: 10.1002/jmri.20698.

[37] R. Wood, K. Bassett, V. Foerster, et al., *1.5 Tesla Magnetic Resonance Imaging Scanners Compared with 3.0 Tesla Magnetic Resonance Imaging Scanners: Systematic Review of Clinical Effectiveness*. Ottawa, ON, Canada: Canadian Agency for Drugs and Technologies in Health, 2011. [Online]. Available: https://www.ncbi.nlm.nih.gov/books/NBK174456/.

[38] O. S. Mian, Y. Li, A. Antunes, P. M. Glover, and B. L. Day, "On the vertigo due to static magnetic fields," *PLoS ONE*, vol. 8, no. 10, e78748, 2013, Available at: https://pmc.ncbi.nlm.nih.gov/articles/PMC3813712/. DOI: 10.1371/journal.pone.0078748. Accessed: Feb. 20, 2026.

[39] J. P. D. Wilde, D. Grainger, D. L. Price, and C. Renaud, "Magnetic resonance imaging safety issues including an analysis of recorded incidents within the uk," *Progress in Nuclear Magnetic Resonance Spectroscopy*, vol. 51, no. 1, pp. 37–48, 2007. DOI: 10.1016/j.pnmrs.2007.01.003.

[40] L. P. Panych and B. Madore, "The physics of mri safety," *Journal of Magnetic Resonance Imaging*, vol. 47, no. 1, pp. 28–43, 2018. DOI: 10.1002/jmri.25761. [Online]. Available: https://pubmed.ncbi.nlm.nih.gov/28543948/.

[41] B. A. Hargreaves, P. W. Worters, K. B. Pauly, J. M. Pauly, K. M. Koch, and G. E. Gold, "Metal-induced artifacts in mri," *American Journal of Roentgenology*, vol. 197, no. 3, pp. 547–555, Sep. 2011. DOI: 10.2214/AJR.11.7364.

[42] G. Fierens, N. Standaert, R. Peeters, C. Glorieux, and N. Verhaert, "Safety of active auditory implants in magnetic resonance imaging," *Hearing Research*, vol. 395, p. 107 919, 2020. DOI: 10.1016/j.heares.2020.107919.

[43] ASTM International, *Astm f2503-20: Standard practice for marking medical devices and other items for safety in the magnetic resonance environment*, West Conshohocken, PA: ASTM International, 2020.

[44] M. Andersson, *Property Requirements for Medical Implant Materials*, Department of Chemistry, Chalmers, Gothenburg, Nov. 2025. Accessed: Feb. 10, 2026.

[45] D. F. Williams, "There is no such thing as a biocompatible material," en, *Biomaterials*, vol. 35, no. 38, pp. 10 009–10 014, Dec. 2014, ISSN: 01429612. DOI: 10.1016/j.biomaterials.2014.08.035. Accessed: Feb. 10, 2026. [Online]. Available: https://linkinghub.elsevier.com/retrieve/pii/S0142961214009600.

[46] L. Lebea, R. Sigwadi, T. Pandelani, and F. Nemavhola, "Mechanical Compatibility Is the New Biocompatibility: A Process View of Implant Success," en, *Processes*, vol. 14, no. 3, p. 505, Feb. 2026, ISSN: 2227-9717. DOI: 10.3390/pr14030505. Accessed: Feb. 12, 2026. [Online]. Available: https://www.mdpi.com/2227-9717/14/3/505.

[47] R. Sheposh, *Young's modulus*, en, 2024. Accessed: Feb. 12, 2026. [Online]. Available: https://www.ebsco.com/research-starters/history/youngs-modulus.

[48] M. Niinomi, Y. Liu, M. Nakai, H. Liu, and H. Li, "Biomedical titanium alloys with Young's moduli close to that of cortical bone," eng, *Regenerative*

Biomaterials, vol. 3, no. 3, pp. 173–185, Sep. 2016, ISSN: 2056-3418. DOI: 10.1093/rb/rbw016.

[49] M. Pawlaczyk, M. Lelonkiewicz, and M. Wieczorowski, "Age-dependent biomechanical properties of the skin," vol. 30, no. 5, pp. 302–306, Oct. 2013, ISSN: 1642-395X. DOI: 10.5114/pdia.2013.38359. Accessed: Feb. 10, 2026. [Online]. Available: https://www.ncbi.nlm.nih.gov/pmc/articles/PMC3858658/.

[50] A. Trotta and A. Ní Annaidh, "Mechanical characterisation of human and porcine scalp tissue at dynamic strain rates," eng, *Journal of the Mechanical Behavior of Biomedical Materials*, vol. 100, p. 103 381, Dec. 2019, ISSN: 1878-0180. DOI: 10.1016/j.jmbbm.2019.103381.

[51] J. Zwirner, B. Ondruschka, M. Scholze, G. Schulze-Tanzil, and N. Hammer, "Load-deformation characteristics of acellular human scalp: Assessing tissue grafts from a material testing perspective," eng, *Scientific Reports*, vol. 10, no. 1, p. 19 243, Nov. 2020, ISSN: 2045-2322. DOI: 10.1038/s41598-020-75875-z.

[52] L. Falland-Cheung et al., "Mechanical properties of the human scalp in tension," eng, *Journal of the Mechanical Behavior of Biomedical Materials*, vol. 84, pp. 188–197, Aug. 2018, ISSN: 1878-0180. DOI: 10.1016/j.jmbbm.2018.05.024.

[53] J. J. Chruściel, "Most Important Biomedical and Pharmaceutical Applications of Silicones," en, *Materials*, vol. 18, no. 11, p. 2561, May 2025, ISSN: 1996-1944. DOI: 10.3390/ma18112561. Accessed: Feb. 12, 2026. [Online]. Available: https://www.mdpi.com/1996-1944/18/11/2561.

[54] K. Isogai et al., "Young's moduli of subcutaneous tissues and muscles under different loads at the gluteal region calculated using ultrasonography," en, *Journal of Physical Therapy Science*, vol. 34, no. 12, pp. 777–783, 2022, ISSN: 0915-5287, 2187-5626. DOI: 10.1589/jpts.34.777. Accessed: Feb. 12, 2026. [Online]. Available: https://www.jstage.jst.go.jp/article/jpts/34/12/34_2022-063/_article.

[55] K. Mondal, G. Kaur, and R. C. Advincula, "Advanced silicone materials for soft actuator applications," en, *RSC Applied Polymers*, vol. 4, no. 1, pp. 12–29, 2026, ISSN: 2755-371X. DOI: 10.1039/D5LP00290G. Accessed: Feb. 12, 2026. [Online]. Available: https://xlink.rsc.org/?DOI=D5LP00290G.

[56] L. W. McKeen, *Fatigue and Tribological Properties of Plastics and Elastomers*, 3rd ed. William Andrew, 2016, ISBN: 9780323442015.

[57] I. M. Meththananda, S. Parker, M. P. Patel, and M. Braden, "The relationship between shore hardness of elastomeric dental materials and young's modulus," *Dental Materials*, vol. 25, no. 8, pp. 956–959, 2009.

[58] I. M. Meththananda, S. Parker, M. P. Patel, and M. Braden, "The relationship between Shore hardness of elastomeric dental materials and Young's modulus," *Dental Materials*, vol. 25, no. 8, pp. 956–959, Aug. 2009, ISSN: 0109-5641. DOI: 10.1016/j.dental.2009.02.001. Accessed: Mar. 16, 2026. [Online]. Available: https://www.sciencedirect.com/science/article/pii/S0109564109001237.

[59] *Euler-Bernoulli Beam Theory - an overview | ScienceDirect Topics*. Accessed: Feb. 10, 2026. [Online]. Available: https://www.sciencedirect.com/topics/materials-science/euler-bernoulli-beam-theory.

[60] D. M. Parks, *Euler-Bernoulli Beams: Bending, Buckling, and Vibration*, Department of Mechanical Engineering, MIT, Feb. 2004. Accessed: Feb. 10, 2026. [Online]. Available: https://www.scribd.com/document/356050594/Euler-Bernoulli-Equation.

[61] *Area Moment of Inertia with Definitions, Formulas & Calculator*. [Online]. Available: https://www.engineeringtoolbox.com/area-moment-inertia-d_1328.html#:~:text=Solid%20Square%20Cross%20Section,%2D%20h3)%20(8).

[62] *Stress Concentration - an overview | ScienceDirect Topics*. Accessed: Apr. 7, 2026. [Online]. Available: https://www.sciencedirect.com/topics/materials-science/stress-concentration?utm_source=chatgpt.com.

[63] M. F. El-Amin, *Numerical Modeling of Nanoparticle Transport in Porous Media*. Elsevier, 2023. DOI: https://doi.org/10.1016/B978-0-323-90511-4.00005-8.

[64] *Ls-dyna theory manual*, Version R16, Ansys Inc., 2025. [Online]. Available: https://lsdyna.ansys.com/wp-content/uploads/2025/04/LS-DYNA_Manual_Theory_R16.pdf.

[65] D. Kreculj and B. Rasuo, "Impact damage modeling in laminated composite aircraft structures," in *Sustainable Composites for Aerospace Applications*, Woodhead Publishing, 2018, pp. 125–153. DOI: 10.1016/B978-0-08-102131-6.00007-4.

[66] *LS-DYNA Keyword User's Manual*, Volume III, Mar. 2001. Accessed: Mar. 9, 2026. [Online]. Available: https://ftp.lstc.com/anonymous/outgoing/jday/manuals/ls-dyna_960_manual_s.pdf.

[67] R. Keerthiwansa, J. Javořík, S. Rusnáková, J. Kledrowetz, and P. Gross, "Hyperelastic Material Characterization: How the Change in Mooney-Rivlin Parameter Values Effect the Model Curve," en, *Materials Science Forum*, vol. 994, pp. 265–271, 2020, ISSN: 1662-9752. DOI: 10.4028/www.scientific.net/MSF.994.265. Accessed: Mar. 9, 2026. [Online]. Available: https://www.scientific.net/MSF.994.265.

[68] Y. Dong, R. Lin, and D. Bhattacharyya, "Determination of critical material parameters for numerical simulation of acrylic sheet forming," *Journal of Materials Science*, vol. 40, pp. 399–410, Aug. 2005. DOI: 10.1007/s10853-005-6096-0.

[69] M. L. Wang and G. Wang, "Electromagnetic sensors for assessing and monitoring civil infrastructures," in *Electromagnetic Sensors for Assessing and Monitoring Civil Infrastructures*, Elsevier, 2018. DOI: 10.1016/B978-0-08-102696-0.00015-4.

[70] *Can you shield or block magnetic fields? | Science Guys | Union University, a Christian College in Tennessee*. Accessed: Mar. 19, 2026. [Online]. Available: https://www.uu.edu/dept/physics/scienceguys/2004Feb.cfm#:~:text=The%20short%20answer%20is%20no,way%20back%20to%20their%20origin..

[71] *Permeability of Vacuum - an overview | ScienceDirect Topics*. Accessed: Mar. 31, 2026. [Online]. Available: https://www.sciencedirect.com/topics/engineering/permeability-of-vacuum.

[72] B. D. Cullity and C. D. Graham, *Introduction to Magnetic Materials*, 2nd. Piscataway, NJ, USA: Wiley-IEEE Press, 2008.

[73] A. J. Petruska and J. J. Abbott, "Optimal permanent-magnet geometries for dipole field approximation," *IEEE Transactions on Magnetics*, vol. 49, no. 2, pp. 811–819, Feb. 2013. DOI: 10.1109/TMAG.2012.2205014.

[74] *Pain Pressure Threshold (PPT)*, en. Accessed: Apr. 28, 2026. [Online]. Available: https://www.apta.org/patient-care/evidence-based-practice-resources/test-measures/pain-pressure-threshold-ppt.

[75] K. Jensen, H. Ø. Andersen, J. Olesen, and U. Lindblom, "Pressure-pain threshold in human temporal region. evaluation of a new pressure algometer," *Pain*, vol. 25, no. 3, pp. 313–323, 1986. DOI: 10.1016/0304-3959(86)90235-6.

[76] H. Suzuki et al., "Reference intervals and sources of variation of pressure pain threshold for quantitative sensory testing in a Japanese population," en, *Scientific Reports*, vol. 13, no. 1, p. 13 043, Aug. 2023, ISSN: 2045-2322. DOI: 10.1038/s41598-023-40201-w. Accessed: Apr. 28, 2026. [Online]. Available: https://www.nature.com/articles/s41598-023-40201-w.

[77] S. Andersen, M. W. Petersen, A. S. Svendsen, and P. Gazerani, "Pressure pain thresholds assessed over temporalis, masseter, and frontalis muscles in healthy individuals, patients with tension-type headache, and those with migraine–a systematic review," *Pain*, vol. 156, no. 8, pp. 1409–1423, 2015. DOI: 10.1097/j.pain.0000000000000219.

A

Appendix

More images of implant with different wire diameters.

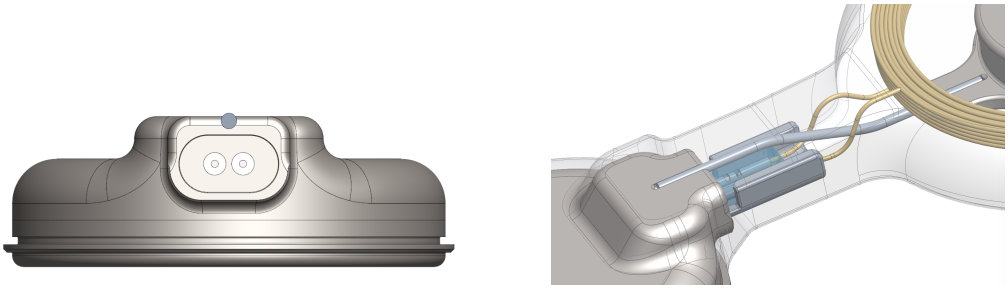

Figure A.1: Implant with reinforcement wire diameter 0.7 mm

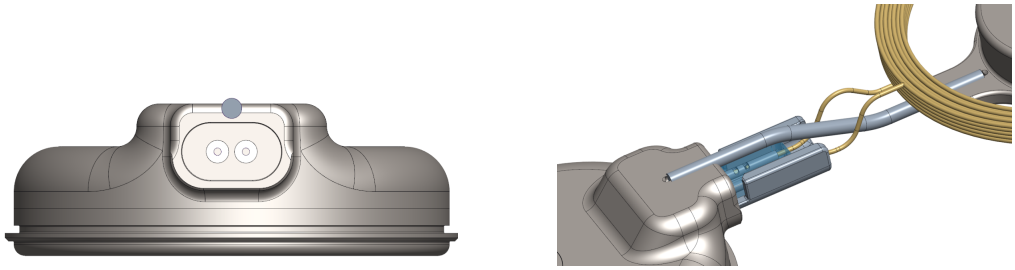

Figure A.2: Implant with reinforcement wire diameter 0.9 mm

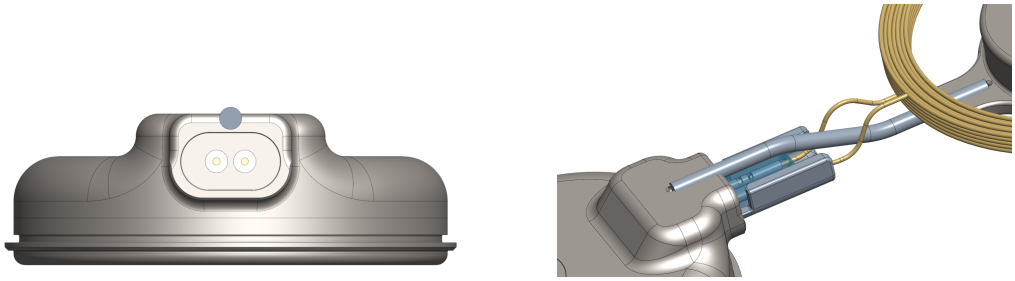

Figure A.3: Implant with reinforcement wire diameter 1.0 mm

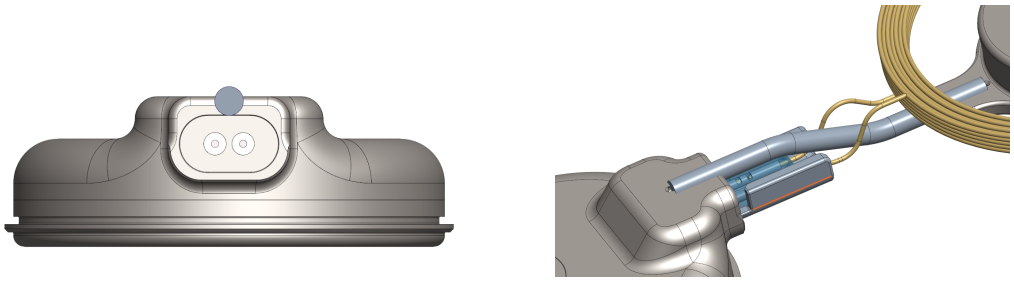

Figure A.4: Implant with reinforcement wire diameter 1.3 mm

DEPARTMENT OF ELECTRICAL ENGINEERING
CHALMERS UNIVERSITY OF TECHNOLOGY
Gothenburg, Sweden
www.chalmers.se

CHALMERS
UNIVERSITY OF TECHNOLOGY